# Integrative spatial analysis reveals tumor heterogeneity and immune colony niche related to clinical outcomes in small cell lung cancer

Graphical abstract

Authors

Haiquan Chen, Chaoqiang Deng, Jian Gao, ..., Yuan Li, Yang Zhang, Zhiwei Cao

Correspondence

hqchen1@yahoo.com (H.C.),
fdudengcq@163.com (C.D.),
luwangjialei@126.com (J.W.),
lumoxuan2009@163.com (Y.L.),
fduzhangyang1987@hotmail.com (Y.Z.),
zwcao@fudan.edu.cn (Z.C.)

In brief

Chen et al. depict the comprehensive single-cell resolved spatial atlas of SCLC. Spatial analyses identify specific multi-positive tumor cell enriched neighborhood which correlates with aggressive pattern and transition trajectory. ColonyMap algorithm further reveals a spatial-clustered immune niche (MT^2) featured as prognostic and predictive potential of informing immunotherapy response.

Highlights

- A spatial atlas comprising CODEX and multi-omics profiles for 165 SCLC patients

- Cellular neighborhoods suggest tumor phenotypic transition and TME changes

- The ColonyMap algorithm detects MT^2 niche highly correlated with superior survival

- M1-like macrophage-based MT^2 niche predicted improved immunotherapy response

Cancer Cell

CellPress

Article

Integrative spatial analysis reveals tumor heterogeneity and immune colony niche related to clinical outcomes in small cell lung cancer

Haiquan Chen,[1,2,3,10,*] Chaoqiang Deng,[1,2,3,10,*] Jian Gao,[1,2,3,10] Jun Wang,[4,10] Fangqiu Fu,[1,2,3,10] Yue Wang,[2,3,5,10] Qiming Wang,[4] Mou Zhang,[4] Shiyue Zhang,[4] Fanfan Fan,[1,2,3] Kun Liu,[1,2,3] Bo Yang,[6] Qiming He,[6] Qiang Zheng,[2,3,5] Xuxia Shen,[2,3,5] Jin Wang,[7] Tao Hu,[7] Changbin Zhu,[7] Fei Yang,[8] Yonghong He,[6] Hong Hu,[1,2,3] Jialei Wang,[9,*] Yuan Li,[2,3,5,*] Yang Zhang,[1,2,3,*] and Zhiwei Cao[4,11,*]

[1]Department of Thoracic Surgery and State Key Laboratory of Genetic Engineering, Fudan University Shanghai Cancer Center, Shanghai 200032, China
[2]Institute of Thoracic Oncology, Fudan University, Shanghai 200032, China
[3]Department of Oncology, Shanghai Medical College, Fudan University, Shanghai 200032, China
[4]School of Life Sciences, Fudan University, Shanghai 200032, China
[5]Department of Pathology, Fudan University Shanghai Cancer Center, Shanghai 200032, China
[6]Department of Life and Health, Shenzhen International Graduate School, Tsinghua University, Shenzhen 518055, China
[7]Department of Translational Medicine, Amoy Diagnostics Co., Ltd, Xiamen 361000, China
[8]Janssen China Research & Development, Shanghai 200233, China
[9]Department of Thoracic Medical Oncology, Fudan University Shanghai Cancer Center, Shanghai 200032, China
[10]These authors contributed equally
[11]Lead contact
*Correspondence: hqchen1@yahoo.com (H.C.), fdudengcq@163.com (C.D.), luwangjialei@126.com (J.W.), lumoxuan2009@163.com (Y.L.), fduzhangyang1987@hotmail.com (Y.Z.), zwcao@fudan.edu.cn (Z.C.)
https://doi.org/10.1016/j.ccell.2025.01.012

SUMMARY

Recent advances have shed light on the molecular heterogeneity of small cell lung cancer (SCLC), yet the spatial organizations and cellular interactions in tumor immune microenvironment remain to be elucidated. Here, we employ co-detection by indexing (CODEX) and multi-omics profiling to delineate the spatial landscape for 165 SCLC patients, generating 267 high-dimensional images encompassing over 9.3 million cells. Integrating CODEX and genomic data reveals a multi-positive tumor cell neighborhood within ASCL1+ (SCLC-A) subtype, characterized by high SLFN11 expression and associated with poor prognosis. We further develop a cell colony detection algorithm (ColonyMap) and reveal a spatially assembled immune niche consisting of antitumoral macrophages, CD8+ T cells and natural killer T cells (MT^2) which highly correlates with superior survival and predicts improving immunotherapy response in an independent cohort. This study serves as a valuable resource to study SCLC spatial heterogeneity and offers insights into potential patient stratification and personalized treatments.

INTRODUCTION

Small cell lung cancer (SCLC) is an aggressive malignancy characterized by rapid growth, early dissemination, and generally dismal long-term prognosis.[1] Despite initial response to platinum-based chemotherapy, it rapidly acquires resistance and disease progression. While immunotherapy recently shed light on a potential breakthrough for SCLC treatment,[2] the survival benefit was only observed for a selected group of patients. In contrast to the biomarker-directed personalized treatment strategies in other cancers, such as non-small cell lung cancer (NSCLC)[3–5] and breast cancer,[6–8] SCLC has long been treated as a homogeneous disease. Until recently, large-scale bulk gene expression analyses suggested the molecular subtypes and intertumoral heterogeneity

of SCLC based on four lineage-defining transcription factors (ASCL1 [SCLC-A], NEUROD1 [SCLC-N], POU2F3 [SCLC-P], and YAP1 [SCLC-Y]).[9–11] The latest bulk proteogenomic study identified four alternative subtypes from 112 SCLC patients and suggested their potential distinct therapeutic vulnerabilities validated on cell line and cell line-derived xenograft (CDX)/patient-derived xenograft (PDX) models.[12] In addition to the aforementioned intertumoral differences, intratumoral heterogeneity of SCLC was also investigated by time-series single-cell transcriptome (scRNA-seq) analysis in genetically engineered mouse models (GEMMs), which uncovered the coexistence of multiple molecular subtypes within individual tumor, linking to potential therapeutic selectivity.[13,14]

The aforementioned genomic and transcriptomic analysis at bulk and single-cell levels has significantly improved the depth

of SCLC heterogeneity and proposed promising therapeutic selections. Yet, the spatial-resolved inter- and intratumoral heterogeneity, cellular organization, and their relationships with patient outcomes remain largely unexplored in SCLC. The advent of highly multiplexed imaging technologies such as co-detection by indexing (CODEX) allows capturing layered molecular parameters of single cells while preserving their spatial geographical information in formalin-fixed, paraffin-embedded (FFPE) tissues, enabling incorporating long-term follow-up data from a single-cell resolved spatial perspective.[15,16] Through *in situ* analysis, cellular functional "states", spatial interaction, as well as cellular neighborhood (CN) could be investigated simultaneously.[17–20] For instance, specific cellular interactions exist across different histological subtypes of lung adenocarcinoma.[19] And antitumoral immunity-related CNs have been identified with CODEX in colorectal cancer and melanoma.[18,21] To date, however, there is still a scarcity of spatial geographical atlas resources incorporating tumor-immune interactions with prognosis and treatment response for SCLC.

In this paper, CODEX technology was leveraged with a 35-plex antibody panel in limited-stage SCLC patients from the Fudan University Human Lung Tissue Multi-omics Atlas (HLTMA) cohort, a clinically annotated set with standardized tissue acquisition and multi-omics profiling pipeline. Our study generated 267 high-dimensional images along with whole-exome, *in situ* single-cell resolved RNA and bulk RNA sequencing data for 165 SCLC patients. Through systematic, geographical analysis, we resolved more than 9.3 million cells, identified striking intratumoral molecular heterogeneity, and depicted spatial CN transition trajectory accompanied by distinct immune microenvironment and genomic profiles. To better explore spatial organization and cellular interaction, we further developed ColonyMap algorithm and discovered a spatial-clustered niche of antitumoral immune cells, which were predictive of SCLC patient survival and immunotherapy response. Taken together, our curated data and analytical techniques serve as a valuable resource as well as framework for further oncology research.

RESULTS

Spatially resolved single-cell phenotypic atlas in SCLC
To comprehensively profile the cellular composition, spatial organization, and molecular heterogeneity of SCLC, we created a multi-omics atlas of primary SCLC tumors representing all clinicopathological characteristics (Fudan University [FU]-SCLC cohort) from the HLTMA cohort (Table S1) with long-term follow-up data (median follow up: 62.3 months; interquartile range: 36.1–113.0 months). For this study, tumor tissues before systemic therapy were used for whole-exome sequencing (WES), bulk RNA sequencing (RNA-seq), and CODEX, with spatial molecular imager (SMI) CosMx and immunohistochemical (IHC) staining validation (Figures 1A and S1). A 35-plex antibody panel (Table S2) for CODEX was designed to simultaneously quantified proteins including molecular subtyping transcription factors (TFs) for SCLC heterogeneity; markers of epithelial, mesenchymal, immune, and endothelial lineages for the tumor microenvironment (TME); and targets for cell functional status or undergoing clinical drug trials[22–25] (Figure 1B). We acquired 267 high-dimensional histopathology images

from 129 tumor samples and 16 paired adjacent normal tissues (Figures 1C and S1). In total, we detected 9,337,647 cells and used a supervised lineage assignment approach to classify cell phenotypes based on canonical markers (Figures 1D and 1E). Markers which expressed both in tumor cells (TCs) as well as immune cells were well identified for accurate annotation (Figure S1D). For instance, double-negative T (dnT) was defined as $CD3^+CD4^-CD8^-CD56^-$ T cell. Natural killer T cell (NKT) was defined as $CD3^+CD4^-CD8^-CD56^+$ T cell, and $CD3^-CD56^+$ cell was annotated as natural killer (NK) cell (Figure S1C). In particular, multi-positive tumor cells (MPTC) were detected with phenotype of co-expressing two or more positive TF markers (Figure 1E). Almost all tumors (120 of the 129 tumors) imaged by CODEX were sampled at least two cores (one core for nine tumors and three cores for two tumors), which allowed us to explore spatial intratumor heterogeneity (Figure S2). Tumor composition was better conserved across cores than were TME cell phenotypes, although exceptions existed. For instance, the correlation of $YAP1^+$ TCs was relatively weak, possibly due to the nonspecific expression pattern of YAP1 between tumor and mesenchymal tissues (Figure S1D). While $CD68^+$ macrophages were well conserved between cores from the same tumor, indicating its relative strong ability of tumor infiltrating. In conclusion, heterogeneity existed in the tumor and immune microenvironment across different regions in SCLC, and spatial omics offered advantages of domain segmentation and architecture mapping over conventional bulk sequencing.

CODEX queried layers of tumor heterogeneity in SCLC
Recent researches performing IHC on FFPE tissue sections have suggested the potential co-expression of two or more TF markers in the same SCLC tumor sample.[26–28] It is worthy to explore the further details of molecular and TME heterogeneity at single cell level. We calculated the cellular proportions of various TCs and immune cells (Table S1). $ASCL1^+$ TCs accounted for more than 50% of all TCs, while macrophages were the most abundant among immune cells. Strikingly, over 10% of TCs (916,348 cells) were identified as MPTCs (Figures 2A and 2B). Validation was done through IHC (Figures 2B and S3A), scRNA-seq (Figure S3B), and SMI CosMx (Figure S3C) on serial sections and confirmed the existence of MPTCs. Among these MPTCs, co-expression of ASCL1 and NEUROD1 was most prevalent, followed by $ASCL1^+YAP1^+$ and $NEUROD1^+$ $YAP1^+$ cells, with a minor fraction exhibiting $ASCL1^+NEUROD1^+$ $YAP1^+$ phenotype. POU2F3 expression was nearly mutually exclusive with ASCL1 and NEUROD1, while YAP1 displayed a more ubiquitous expression pattern (Figure 1E). Recent studies employing GEMMs have elucidated a phenotypic neuroendocrine (NE) dedifferentiation trajectory from ASCL1 to NEUROD1 to YAP1 in SCLC.[14] The $POU2F3^+$ cells, conversely, derived from a distinct tuft cell lineage, corroborating our single-cell resolution findings.[11,29] When analyzing each core, we adopted a strategy analogous to pathological subtyping in lung adenocarcinoma, whereby 5% was chosen as the minimum threshold and the predominant molecular subtype was defined as the phenotype with highest proportion. MPTCs were enumerated separately across respective phenotypic categories. For instance, a patient harboring 60% $ASCL1^+$ TCs and 20% mixed $ASCL1^+NEUROD1^+$ TCs would be classified as the SCLC-A

# Cancer Cell
Article

CellPress
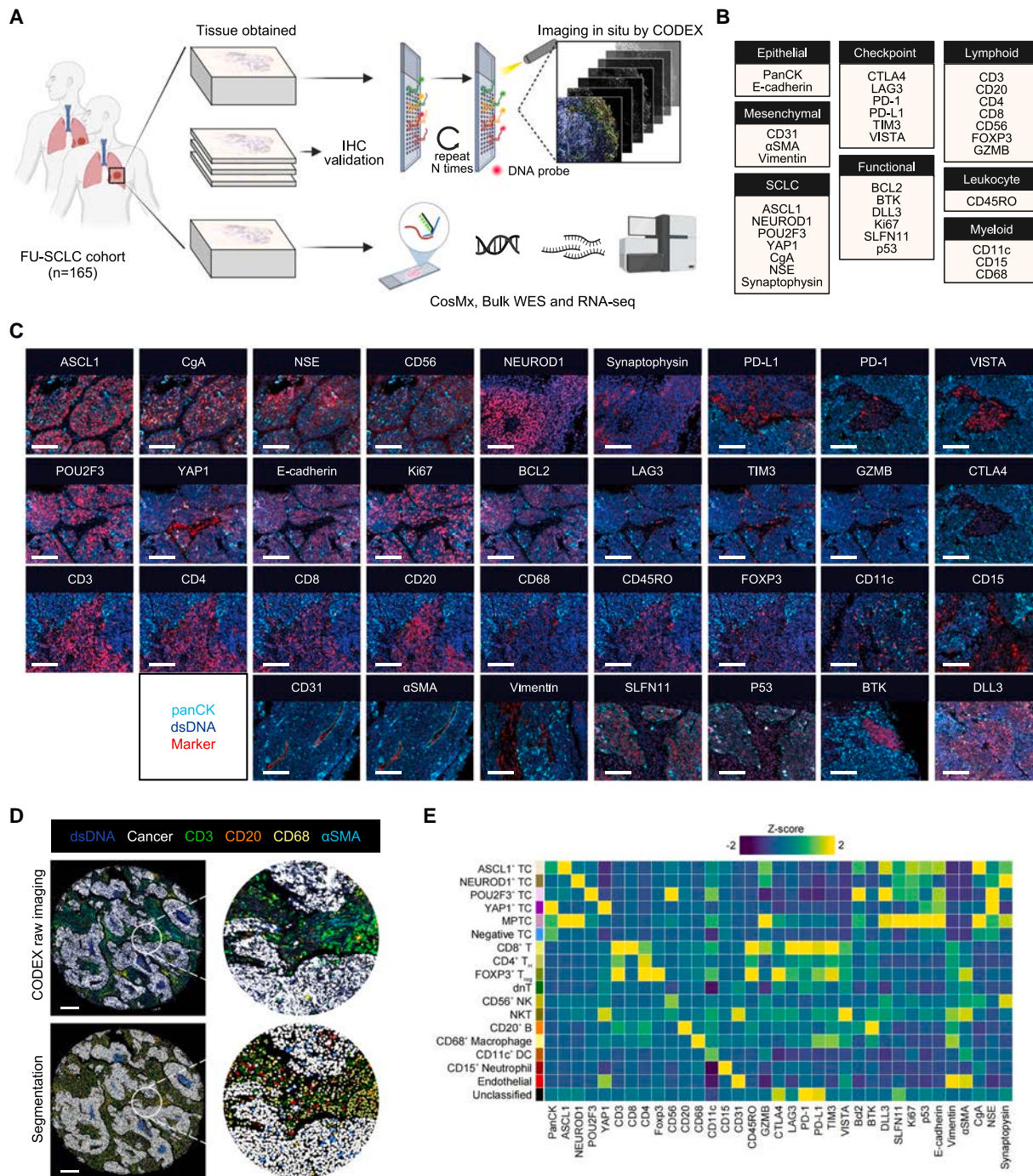
Figure 1. CODEX and multi-omics workflow in FU-SCLC cohort

(A) Depiction of the parallel tissue analysis methods in FU-SCLC cohort, including IHC staining, bulk WES and RNA-seq, SMI CosMx and high-dimensional CODEX imaging, with an overview of the CODEX.

(B) Markers used in the CODEX panel, grouped by target cell type or protein class.

(C) Representative examples of CODEX image data (cropped to fit); scale bar, 50 μm.

(D) Representative CODEX image of one tumor core with a six-color overlay of cancer and immune cell lineage markers, and the corresponding cell segmentation mask map showing cell identity by color overlaid onto the mask; scale bar, 250 μm.

(E) Heatmap showing average expression of all markers across cell phenotypes identified by CODEX.

For clarification, MPTC was tumor cell detected with phenotype of co-expressing two or more positive transcription factors. dnT was defined as $CD3^+CD4^-CD8^-CD56^-$ T cell, and NKT was defined as $CD3^+CD4^-CD8^-CD56^+$ T cell. TC, tumor cell; T_H, helper T cell; T_{reg}, regulatory T cell; NK, natural killer; DC, dendritic cell. Also see Figures S1 and S2, Tables S1 and S2
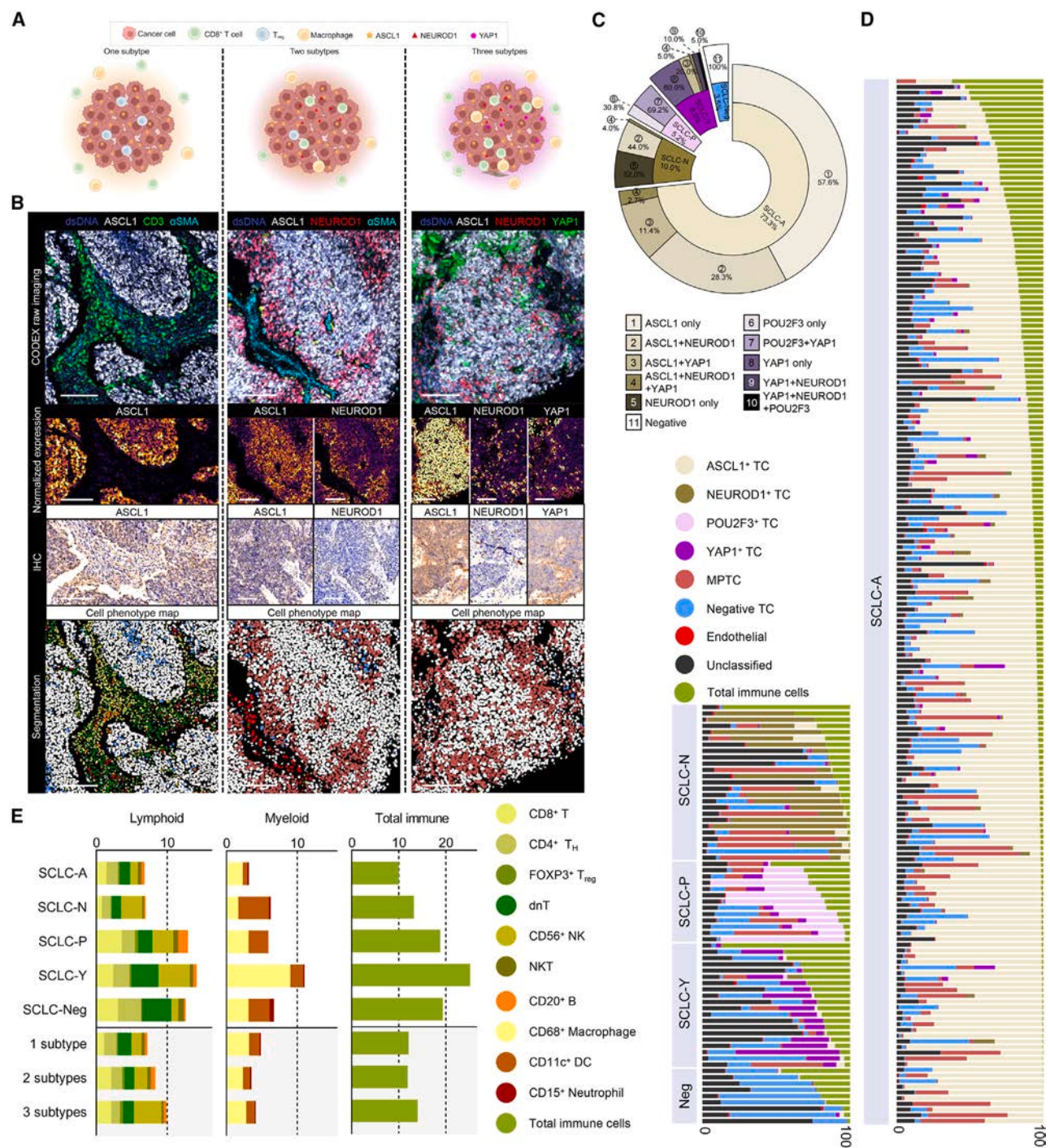
Figure 2. CODEX queried layers of tumor heterogeneity in SCLC

(A) Schematic illustrating co-expression pattern within a single tumor.

(B) Representative CODEX images of a ASCL1+ tumor (left), ASCL1+NEUROD1+ tumor (middle), and ASCL1+NEUROD1+YAP1+ tumor (right). The second panel showing normalized expression of each TF with IHC validation (the third panel). A cell phenotype map overlaid onto the cell segmentation mask (the fourth panel, colors correspond to cell lineages in D and E); scale bar, 100 μm.

(C) Donut charts representing the percentages of SCLC predominant subtypes in each core (inside donut), and percentages of various TF expression combinations (outside donut, with legend) for all five groups shown. Neg, negative.

(D) Waterfall plot depicting the distribution of six tumor cell phenotypes and total immune cell infiltration across each SCLC predominant subtypes at the core level.

(E) Stacked bar graph of the indicated immune cell phenotypes as a percentage of all cells according to SCLC predominant subtypes (upper panel) and to subtype counts (down panel), all at the core level. Also see Figures S3–S5, Tables S1 and S2.

Cancer Cell
Article

CellPress

predominant subtype, while also annotated as ASCL1^{+}/NEUROD1^{+} hybrid subtype (subtype count = 2). In our study, over 40% of SCLC-A cores harbored MPTCs, suggesting a striking intratumoral molecular heterogeneity (Figures 2C and S4A). Correlation analysis revealed a significant negative association between the proportion of ASCL1^{+} TCs and that of NEUROD1^{+}/YAP1^{+} TCs (Figure S4B). Using bulk RNA-seq data, it was observed that in comparison to the SCLC-A predominant subtype, the expression of NE differentiation-associated genes decreases in the SCLC-N/Y subtypes, while non-NE differentiation-associated genes showed the opposite trend (Figure S4C). These suggested that such subtyping strategy potentially characterized the dedifferentiation process in SCLC. Of note, one tumor displayed three subtyping phenotypes: NEUROD1^{+}, YAP1^{+}, and POU2F3[+], a rare case similarly observed by Ireland et al.,[14] warranting further investigation into the cellular origins and evolutionary trajectories of such tumors.

The cellular landscape of the lung tumor immune microenvironment (TIME) was then characterized. Analysis was firstly performed on 16 tumors and paired adjacent normal tissues. The proportions of most immune cell types were not increased in tumor except for CD56^{+} NK cells, compared with adjacent normal tissues (Figure S4D upper panel), supporting the "cold" TIME feature in SCLC. Among the subtypes, SCLC-Y had the greatest immune infiltration (25.2%) (Figures 2D and 2E), and such advantage was mainly driven by shifts within the myeloid compartment, macrophages in particular, with significant differences in the average frequency between SCLC-Y and other subtypes (Figures 2E and S4D middle panel). Interestingly, the frequency of FOXP3^{+} T$_{reg}$ cell clusters was only significantly higher in SCLC-P subtype, despite the entire low frequency of T$_{reg}$ cells in SCLC (Figures 2E and S4D middle panel). Correspondingly, the prognosis of patients with SCLC-P subtype was significantly worse than that of other subtypes, while SCLC-Y correlated with the best survival in our dataset (Figures S4E and S4F). To validate the immune infiltration level of SCLC-Y subtype, four clusters were further identified in bulk RNA-seq data (Figures S5A and S5B). Single SCLC-Y tumors could be observed in cluster 1, combined with SCLC-P. After excluded SCLC-P tumors, cluster 1 showed elevated immune signature scores compared with other clusters (Figure S5C). We also compared the immune infiltration between scRNA-seq samples with a YAP1^{+} TC proportion greater than or equal to 1% and those with that less than 1%. And the former exhibited stronger immune infiltration (Figures S5D and S5E), verifying our CODEX findings. Analysis indicated a relatively high level of immune infiltration in SCLC-Neg tumors (Figure 2E), second only to SCLC-Y tumors. These quadruple-negative TCs were mainly necrotic and shrunken pathologically, which might be suppressed or eliminated by the immune system. Minimal immunological or patient survival difference was unveiled between subtype counts (Figures 2E, S5F, and S5G).

When assessing the relationship between immune cell populations and clinicopathological characteristics, we interrogated the frequency of individual cell types as a percentage of total cells within each patient. Male patients had inferior overall survival (OS) than females in SCLC (Figure S4F), likely related to the significantly higher frequency of endothelial cells (ECs) (Fig-

ure S4D down panel). ECs was found as the only cell type correlating with short-term survival (STS), although many other immune clusters had an enrichment in pathological stage I patients who had better survival than stage II-III patients (Figures S4D down panel and Figure S4F).

In summary, the heterogeneity of molecular marker expression and immune cell composition across several SCLC subtypes was unveiled by CODEX. While tumor-infiltrating lymphocyte frequency was reported with prognostic utility in certain malignancies,[30–33] no significant correlation was detected in our study between single immune subset abundances and survival in SCLC patients, necessitating further interrogation of cellular functional states or higher-dimensional construction profiling.

CNs marked spatial phenotypic transition and survival outcomes

Based on aforementioned cellular frequency and composition analysis, we further explore the cell-cell interactions and TIME from the spatial perspective. Permutation test was firstly performed to quantify interaction preference between cell types across each SCLC subtypes (Figures S5H and S5I). Homotypic interactions were highly prevalent within TCs and immune cell populations, respectively, consistent with interaction analyses in lung adenocarcinoma and breast cancer.[19,34] Within the homotypic T cell interactions, SCLC-N and SCLC-Y subtypes exhibited enriched interactions among CD8^{+} T cells, CD4^{+} T helper (T$_H$) cells, and dnT cells (Figures S5H and S5I, box 1a, 1b). Notably, these T cell interactions, rather than cell proportions, correlated with prolonged patient survival (Figures S4D and S5H, right panel). ECs tended to interact with inflammatory T cells in SCLC-Y tumors compared with other subtypes (Figure S5H, box 2). Interestingly, FOXP3^{+} T$_{reg}$ cells displayed heightened interactions with CD8^{+} T cells or NKT cells in SCLC-P subtype compared with other subtypes (Figure S5H and S5I, box 1a, box 3). Yet these interactions were independent of the overall infiltration of these cell types (Figure S5J).

We next explored how CN organized within the tumor and TIME across SCLC subtypes. A canonical approach[18] was applied to establish 20 CN clusters that recapitulated both new and known TIME architectures (Figures 3A and 3B), including pan-immune (CN1), macrophage enriched (CN12), vascular (CN5), and others. Of note, this CN analysis further stratified the local tumor nests based on the spatial relationships and proportions of each TC, including several MPTC enriched neighborhoods (CN2, CN9, CN13, and CN14). To identify CNs associated with survival, multivariate Cox regression analysis adjusting TNM stages was performed using CN proportions as variables, considering the tumor stage as the important prognostic factor (Figure S6A). Across all patients, neighborhood proportions did not correlate with OS. When restricted to the SCLC-A predominant subtype, CN7 (YAP1^{+} TC enriched), CN9 (MPTC enriched), and CN10 (NEUROD1^{+} TC enriched) exhibited significant association with inferior outcomes, and CN17 (ASCL1^{+} TC enriched) correlated with improved survival (Figure 3B). This suggested that within an ASCL1^{+} predominant tumor, the emergence of other subtypes portended an adverse prognosis. No similar tread was observed in other predominant subtypes (Table S3).

The co-expression of TFs in SCLC has actually been revealed in several studies, while these MPTCs could not be well defined
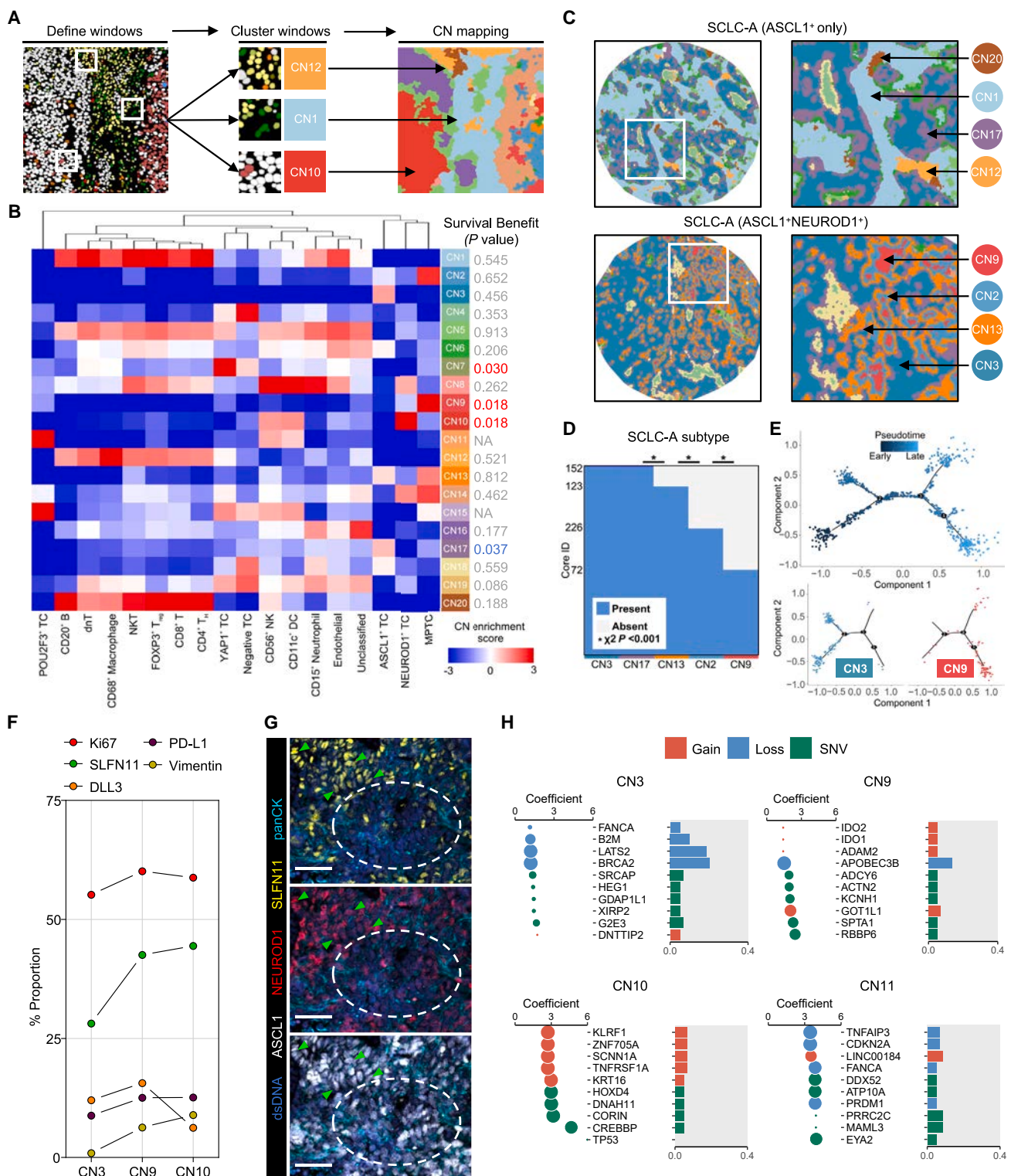
Figure 3. CNs marked spatial phenotypic transition and survival outcomes

(A) Schematic depicting workflow of cellular neighborhood (CN) assignments. Voronoi diagram (right) is used for CN mapping.

(B) Heatmap of cellular compositions represented across CNs (n = 251 images; n = 20 nearest cells; CN = 20 neighborhoods). p values (right) are calculated using multivariate Cox proportional hazards regression model for SCLC-A predominant samples (at the patient level) based on CN frequency, adjusting for pathological TNM stages. The red font denotes an association with inferior prognosis, the blue font, on the contrary.

(C) Representative Voronoi diagrams of CNs for ASCL1^{+} only SCLC-A subtype (upper panel) and ASCL1^{+} NEUROD1^{+} SCLC-A subtype (down panel).

(legend continued on next page)

Cancer Cell
Article

CellPress

in bulk RNA-seq data. Among four MPTC enriched neighborhoods, CN9 was the only structure associated with prognosis. Thus we employed Voronoi mapping to simulate spatial distributions of CNs as visualization (Figures 3C and S6B and S6C). The Voronoi maps aligned well with the original CODEX fluorescence patterns. In hybrid SCLC-A tumors, we observed multiple MPTC enriched neighborhoods arranged in concentric rings, with CN9 centrally located, surrounded by CN2 and CN13, forming a "worm-eaten" pattern (Figure 3C). The CN9 regions corresponded to expression of non-ASCL1 markers. The analyses of occurrence ordering and pseudotime trajectory of each CN were employed, with results indicating CN3 appeared earlier in pseudotime than CN9 (Figures 3D and 3E).

We then performed t-distributed stochastic neighbor embedding (t-SNE) among all MPTCs, and observed distinct expression distribution of several functional markers, such as Ki67 and Schlafen 11 (SLFN11) (Figure S6D). Compared to CN3 which rarely expressed vimentin, a marker for epithelial-mesenchymal transition (EMT), the fraction of vimentin$^+$ TCs was found largely elevated in CN9 (Figure 3F). The proliferative fraction (Ki67$^+$) of TCs in CN9 was also relatively higher than that of CN3. These findings suggested the high proliferative and metastasis potential of TCs during dedifferentiation, partially explaining its relationship with poor prognosis (Figure 3B). scRNA-seq data from SCLC-A subtype cell line-derived murine tumors validated that the proportion of MPTCs was relatively increased in tumors with distant metastasis (Figure S6E and S6F). Considering that vimentin can also characterize dedifferentiation degree, we analyzed CN10 and observed increased expression of vimentin compared with CN3 and CN9 (Figure 3F), aligning well with the linear trajectory hypothesis. Moreover, the fraction of SLFN11$^+$ TCs in CN9 and CN10 was remarkably elevated (Figures 3F and 3G). SLFN11 is a DNA/RNA helicase that sensitizes cancer cells to DNA-damaging agents and has also been identified as a key predictor of poly ADP-ribose polymerase inhibitors (PARPi).[35–37] Previous reports confirmed a bimodal expression pattern of SLFN11 within SCLC-A tumors.[10] Our findings suggested that SLFN11 expression might accompany the dedifferentiation trajectory in SCLC, and the SLFN11$^+$ MPTC proportion might be considered in future PARPi clinical trial designation.

Meanwhile, the relationship between CNs and genomic alterations was explored from perspectives of somatic mutation and copy number variation (CNV) (Figure 3H). We first averaged the targeted CN proportions from each core within the same tumor, and subsequently correlated these averages with genetic events. CN3 was less correlated with somatic mutations but enriched for BRCA2[38–40] and B2M loss, the latter of which may mediate tumor immune escape and immune checkpoint

blockade (ICB) resistance.[41,42] While CN9 harbored the most RBBP6 mutations which was reported to induce EMT process and promote tumor metastasis.[43] CREBBP alterations was the top hit for NEUROD1$^+$ TC enriched neighborhood (CN10) and might associated with SCLC relapse following chemotherapy.[44] Additionally, EYA2 mutation was found to associate with CN11, an SCLC-P subtype enriched cluster (Figure 3H). EYA2 was previously identified as a key regulator that elevated MYC expression and mediates immune evasion in TCs,[45,46] echoing the high T$_{reg}$ frequency in SCLC-P subtype.

In brief, these results suggested a special MPTC enriched neighborhood (CN9) characterized by high metastasis potential, high SLFN11 expression and association with poor prognosis in SCLC-A tumors. This architecture might be correlated with particular somatic alterations, such as RBBP6 which was also known as a p53 negative regulator.[47] And the detailed relationship between CN9 architecture and alterations of p53 and RBBP6 in SCLC warrants further investigation.

ColonyMap detected spatially assembled colonies of SCLC

The CN analysis provided an efficient strategy to describe cellular composition in local microenvironment surrounding each cell.[18] Spatially, the same cell type in aggregated or dispersed states may exhibit distinct physiological functions within tissues. Here, we defined those aggregated homogeneous cells as cell colony, to better study the spatial interaction from the perspective of cell population. Accordingly, ColonyMap, a spatial colony detection algorithm was developed to analyze CODEX and SMI CosMx data. As illustrated in Figure 4A, each colony and its boundary were firstly delineated using image segmentation and a Contour recognition algorithm (see STAR Methods). Then, the overlapping area of different colonies was determined as the colony-colony interaction (CCI) zone, and was analyzed further.

Within our SCLC cohort, ColonyMap accurately detected the tumor and immune boundary in comparison to hematoxylin and eosin (H&E) and CODEX image (Figure 4B). Tertiary lymphoid structure (TLS)-like structures and vessels were also successfully depicted (Figures 4B and S7A). Further comparision between ColonyMap with a commonly used artificial neural network-multilayer perceptron (ANN-MLP) model suggested the reliability of ColonyMap (Figure S7B). 17 colony types were detected from CODEX data. To quantify the spatial distribution of various colonies, the Clark-Evans index[49] was introduced to evaluate their aggregation extent for each patient. The Clark-Evans index is usually used in ecology to quantify the degree of spatial aggregation/dispersion for biological entities within a given area. The distribution of index and colony area were

(D) Presence or absence for five CNs across SCLC-A predominant subtypes at the core level. Chi-square test for p value.
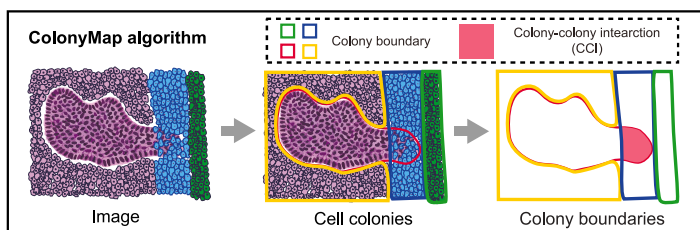
(E) Pseudotime trajectory by Monocle 2 using frequencies of five CNs in (D) as variables (upper panel). Location of indicated CN3 and CN9 projected onto pseudotime space (down panel).

(F) Comparison of functional marker expression among ASCL1$^+$ TCs in CN3, MPTCs in CN9, and NEUROD1$^+$ TCs in CN10. The proportion of marker-positive cells is calculated.
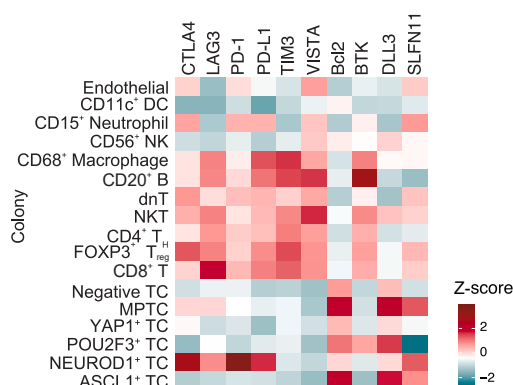
(G) Representative CODEX image overlays of an ASCL1$^+$ NEUROD1$^+$ SCLC showing high expression of SLFN11 in MPTC but not ASCL1$^+$ only region (white dashed line); scale bar, 50 μm.

(H) Top five most enriched somatic mutations or copy-number aberrations in CN3 and CN9 (at the patient level). The targeted CN proportions were averaged from each core within the same tumor. Bubble plots where circles depict coefficients of generalized linear model. Bubble size is inversely proportional to the estimate precision. Bar charts illustrate the proportions of alternations. Also see Figure S5 and S6, Tables S1 and S3.
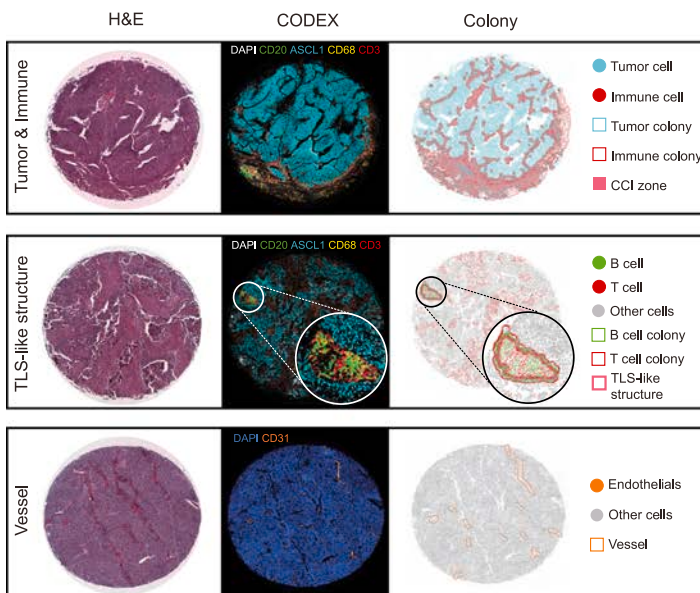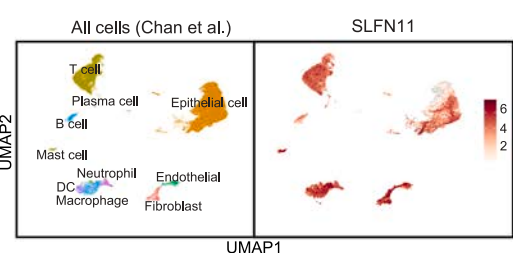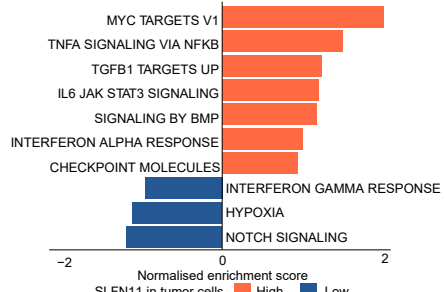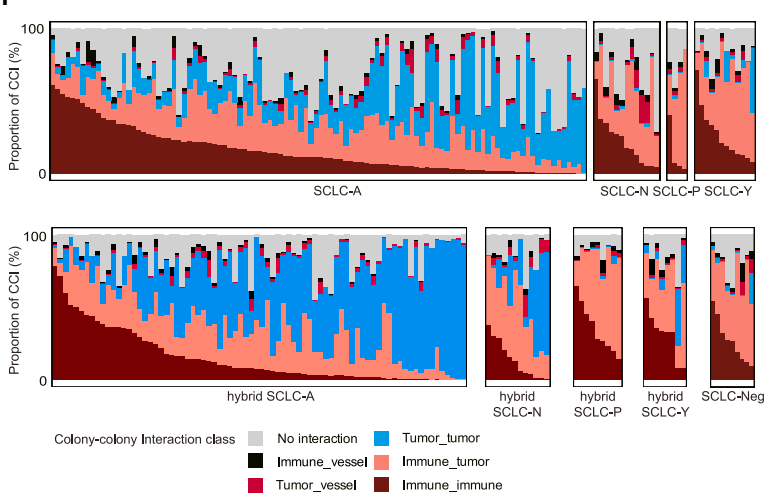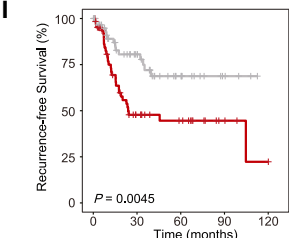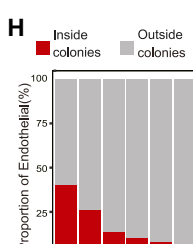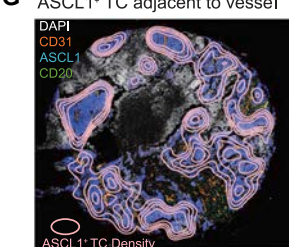
Figure 4. ColonyMap detected spatially assembled colonies of SCLC

(A) Schematic illustration of the ColonyMap algorithm. Original image (left), algorithm-identified colony and boundaries of conspecific cells (center), and extracted boundaries and interaction regions by the algorithm (right).

(B) Tumor and immune boundary, TLS-like structures, and vessels detected by ColonyMap. H&E and CODEX images show tissue staining after marker application. ColonyMap identifies the boundaries of cell colonies. TLS-like regions are defined as areas where T cell colonies encircle B cell colonies.

(C) Heatmap of several immune checkpoints and functional marker expression in 17 cellular colonies.

(legend continued on next page)

Cancer Cell
Article

CellPress

plotted into Kernel density estimation (KDE) maps for cores. Immune cell colonies tended to aggregate smaller than TC colonies (Figure S7C, Table S1).

We first explored the immune checkpoint and functional marker status in each colony (Figure 4C). DLL3 and Bcl2 were mainly expressed in ASCL1+ TC,[10] while SLFN11 was highly expressed in NEUROD1+ TC and MPTC, consistent with the CN results. Interestingly, SLFN11 was also expressed in various immune cells such as CD8+ T cells, which was confirmed in the single-cell data (Figure 4D). SLFN11 has also been reported as a pattern recognition receptor that can significantly regulate microenvironment immune properties.[50] Pathway enrichment analysis indicated that high SLFN11 in TCs activated signaling pathways such as MYC and JAK-STAT, as well as checkpoints (Figures 4E, and S7D and S7E), which had been reported by Lauren et al.[51] Moreover, survival analysis revealed that high SLFN11 in T cells could predict poorer prognosis, outperforming the predictive results of immune checkpoints (Figure S7F).

The colony interactions were then investigated across SCLC subtypes. To provide an overview, the CCIs between colony types were grouped into six classes as immune-immune, immune-tumor, immune-vessel, tumor-tumor, tumor-vessel, and no interaction (Figure 4F). SCLC-A and hybrid SCLC-A displayed more tumor-tumor CCIs than others, indicating their larger intratumoral diversity and spatial complexity. While immune-immune CCIs were more common in SCLC-Y, consistent with the high immune infiltration (Figures 4F and S7G). Surprisingly, ASCL1+ tumor colonies were found to primarily localize adjacent to blood vessels (Figures 4G and S7H), with the highest proportion of ECs inside ASCL1+ colonies compared to others (Figure 4H). More importantly, a lower proportion of CCI between ASCL1+ tumor and EC colonies was significantly associated with better recurrence-free survival (RFS) (p = 0.0045) and OS (p = 0.022) in all SCLC patients (Figures 4I and S7I). Enhanced tumor-vasculature interactions have been reported to be associated with shorter patient survival, considering that newly formed blood vessels can provide essential nutrients to fuel tumor growth, while also serving as conduits for distant dissemination and metastatic lesion establishment.[52]

In SCLC, TCs and immune cells displayed different spatial organization within the TME. Here, our ColonyMap algorithm detected cell colonies and colony interactions based on CODEX data. Such cell colony and CCI analysis may provide new methods and perspectives for discovering clinically relevant sub-structures within the microenvironment.

CCI analysis identified survival-favorable MT² niche

The immune-immune interaction plays a crucial role in the TIME, yet the immune interactions in SCLC have not been systematically studied from a spatial single-cell perspective. Here, we further focused on the immune-immune CCIs particularly, in related to clinical outcomes. Firstly, we analyzed the top five interacting colony types of immune CCI (Figure 5A). T cell exhibited a wide range of interactions with other immune cells. The most abundance in terms of CCI area was observed between T cell and macrophages. Notably, CCI between DC and T cell was scarcely detected, partially related to the low abundance of DCs (Figure 2).

Next, immune CCIs was re-examined according to the detailed 10 immune cell types. The proportion of specific CCI area to overall immune CCI area was illustrated in Figure 5B (upper right panel). As the dash box indicated, macrophage displayed abundant interactions with T cells in general (Figure 5B; Table S4). To test whether this was widespread across cores, the proportion of cores was charted with different colors indicating the prevalence level of the detailed CCI within each core (Figure 5B lower left panel). The results showed that macrophage-related CCIs were indeed prevalent (proportion of this CCI >20%) in majority of cores. The aforementioned results indicated that macrophage and T cells played important roles in TIME of SCLC.

We further explored the detailed CCIs at patient level, correlating with the long-term survival. In contrast to the immune-related CNs, various CCIs showed significant associations with prognosis. To identify potential key players, all binary CCIs including six TCs, 10 immune cells and ECs were scanned. Those were selected if they could significantly distinguish patient prognosis, and were utilized to construct a prognosis-related CCI network, considering both CCI area and proportion (Figure 5C). In this network, a prognosis-favorable colony sub-network was clearly noticed comprising macrophage, NKT, CD8+ T, and T_{reg} cell. Due to the low proportion of T_{reg} cell (<1% of total cells; Table S1), we eventually focused on the immune niche composed of macrophage, NKT and CD8+ T (hereafter referred to as MT²). Strikingly, patients with high area of MT² niche were found to be significantly correlated with favorable long-term survival (p = 0.0049; Figure 5D). High/Low immune infiltration levels failed to distinguish patient prognosis (Figure S8A). However, MT² area seemed to be an independent prognostic factor regardless of overall immune infiltration (Figure 5E). Additionally, MT² maintained the prognostic role in pathological N0 but not in N1-2 patients (Figure S8B). The spatial distribution of MT² niche was then visualized. Interestingly, MT² niche tended to cluster at the boundary of tumor colonies. This phenomenon was particularly clear in MT² niche abundant cores, as Figure 5F (upper panel) displayed. Correspondingly, the OS of MT² niche abundant patients were reported from 40 to 120 months (Figure 5F upper panel). In contrast, Figure 5F

(D) UMAP of all cell subsets from previously published human SCLC scRNA-seq atlas[48] as well as normalized expression of SLFN11 gene.
(E) Pairwise (high vs. low SLFN11 expression in tumor cells annotated in [D]) gene set analyses applying gene signatures corresponding to SCLC neuroendocrine dedifferentiation, interferon response and immune checkpoint.
(F) Waterfall plot depicting the distribution of six CCI classes across each single and hybrid SCLC predominant subtypes.
(G) Colony visualization of ASCL1+ tumor colony localize adjacent to blood vessels.
(H) The proportion of ECs inside or outside each type of TC colony. The proportion of ECs was calculated as the number of ECs inside/outside divided by the total number of ECs in the core.
(I) Kaplan-Meier curve of recurrence-free survival according to area proportion ([ASCL1+ TCs ∩ ECs]/ECs). Patients are classified into two groups based on the median proportion. Also see Figure S7 and Table S1.
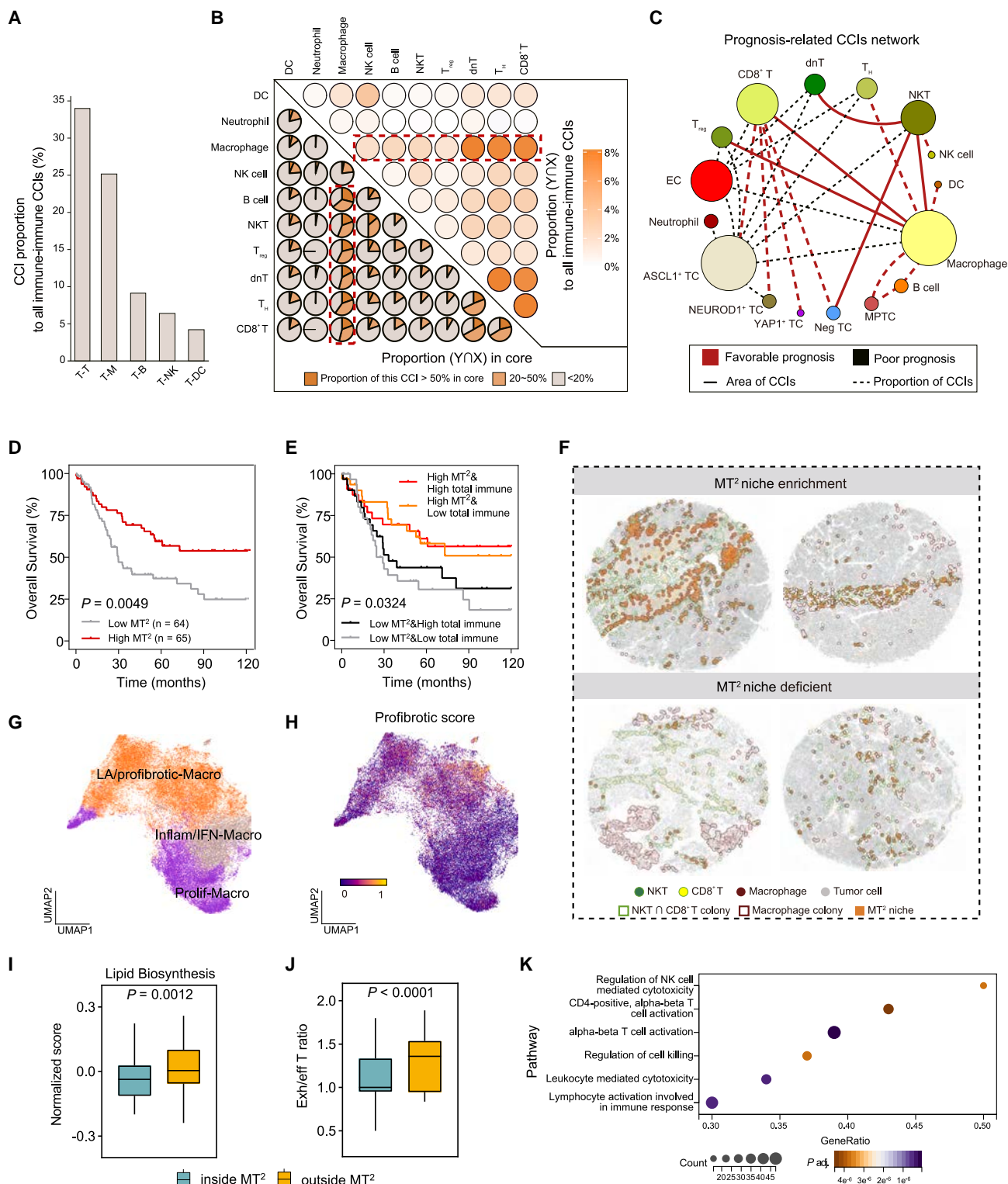
Figure 5. CCI analysis identified survival-favorable MT^2 niche

(A) The area of T cell-related CCIs to area of all immune-immune CCIs.

(B) Detailed cell types in immune CCIs. In the upper-right panel, each circle represents the area (Y ∩ X) to the total immune-immune interaction area. In the lower-left panel, the area (Y ∩ X) is separately calculated within each core. Cores are categorized into three interaction levels based on the ratio of area (Y ∩ X) to the cell type Y area: >50%, 20%–50%, and less than 20%. Finally, a pie chart is used to represent the ratio of cores at different interaction levels out of all cores. The areas

CellPress

(down panel) displayed cores with abundant but disperse macrophages and T cells, instead of assembled MT^2 niche. The corresponding OS of MT^2 deficient patients ranged from 6 to 9 months (Figure 5F down panel).

To investigate the differences in assembled and dispersed states, we then examined and compared functional marker expression in macrophages and T cells inside and outside MT^2 niches. The niche-inside macrophages expressed higher CD11c, suggesting their enhanced antigen-presenting capability compared to the outside ones (Figure S8C). Meanwhile, a significant drop of immune checkpoint markers on CD8$^+$ T cells was observed inside the MT^2 niches, such as PD-1 and CTLA4 (Figure S8C), suggesting reduced T cell exhaustion and immunosuppression in the MT^2 niche. Next, we compared the bulk RNA-seq data at patient level based on MT^2 niche abundance (high/low) and conducted gene set enrichment analysis (GSEA). It was found that the highly expressed genes in MT^2-high group were primarily enriched in macrophage activation, M1/M2 macrophage polarization, and improved lymphocyte chemotactic function, partially explaining why MT^2 area correlated with favorable prognosis (Figure S8D).

Further, the ColonyMap-detected MT^2 niche based on CosMx image confirmed its prognostic value in SCLC (Figure S8E). CosMx data enabled us to explore detailed cell subpopulations and functional states within MT^2 niche, and we employed a consensus model of macrophage subsets,[54] categorizing macrophages into proliferative (Prolif-Macro), lipid-associated/profibrotic (LA/profibrotic-Macro), and M1-like inflammatory/interferon-primed (Inflam/IFN-Macro) subsets (Figure 5G). The LA/profibrotic-Macro were considered immunosuppressive and profibrotic, featured with the idiopathic pulmonary fibrosis (IPF)-associated profibrotic signature[48,53] (Figures 5H and S8F). No significant difference was observed regarding proportions of macrophage and T cell subtypes within and outside of MT^2 (Figure S8G), but distinct functional states were evident. The macrophages within MT^2 exhibited low lipid synthesis, low hypoxia, and elevated antigen presentation capabilities (APC) (Figures 5I and S8H). Additionally, the exhausted T cell index was significantly decreased within MT^2 (Figure 5J). Macrophages within MT^2 were significantly enriched for signaling pathways involved in T cell activation and cytotoxic capabilities (Figure 5K).

In this part, CCI analysis was systematically performed using ColonyMap. An interesting immune-active MT^2 niche was identified, consisting of antigen-presenting macrophages in conjunction with activated cytotoxic T cells and NKT cells, and associated with favorable survival regardless of the overall "immune desert" in SCLC. The distinct functional states of these immune cells suggest a unique local intratumoral microenvironment within SCLC, hinting that the MT^2 niche might influence the immunotherapy response.

M1-like macrophage-based MT^2 niche predicted ICB response

Previously, TIME has often been reported to associate with not only prognosis but also therapeutic responses and efficacy of immunotherapy.[2] Technologies such as scRNA-seq have greatly promoted studies on immune cell subsets and immunotherapy response mechanisms.[55] In SCLC, the ICB outcomes were observed as heterogeneous across patients. There is an urgent need to explore robust immunological markers that help to stratify SCLC patients and predict ICB responses.

We then collected an independent cohort of 23 patients with extensive-stage SCLC (ES-SCLC) who received anti-PD-L1 immunotherapy (atezolizumab or durvalumab). Samples were obtained by tissue biopsy before ICB treatment and we performed multiplex immunofluorescence (mIF) and CosMx on tumor slides for spatial mapping and colony analysis (Figure 6A). Patients were stratified into durable clinical benefit (DCB) and no durable benefit (NDB) groups, evaluated by physician clinically. And the long-term survival after treatment was also selected for ICB efficacy evaluation. Detailed clinicopathological characteristics of this cohort are provided in Table S1. The longest follow-up duration was 33.93 months. Eight patients achieved DCB and 15 patients achieved NDB after ICB therapy.

We employed six immune cell lineage markers including CD86 to distinguish M1-like inflammatory macrophages in mIF tests. The results showed that different cell colonies and MT^2 niches were successfully identified on mIF images, demonstrating the robustness of the ColonyMap approach (Figure 6B). The proportion of neither immune cell colonies nor the MT^2 area differs significantly between the DCB and NDB groups (Figures 6C and S8I). However, when the patients were further stratified into high and low M1-MT^2 group (composed of M1-like CD86$^+$ macrophage, CD8$^+$ T cell and NKT cell), the number of DCB patients was noticed elevated in the high group than the low group (p = 0.089; Figure 6D). Importantly, prognosis analysis revealed that high M1-MT^2 proportion was significantly associated with

---

enclosed by the dashed boxes indicate regions where macrophages exhibit close interactions with various T cell types across both the core and all immune-immune CCI levels.

(C) Prognosis-related CCIs network. Each node represents a cell type, and each edge represents CCIs between two cell types that can significantly distinguish prognosis (p < 0.05). Red/black edges represented favorable/poor prognosis. Patients are grouped using either the proportion of CCIs (dashed line) or the area of CCIs (solid line), with the median serving as the cutoff. Kaplan-Meier analysis is performed after grouping. The diameter of node increases with the number of connected edges.

(D and E) Kaplan-Meier curves according to abundance of MT^2 niche (D) and combination of MT^2 niche and total immune infiltration (E).

(F) Representative mask images of typical MT^2 niche enrichment/deficient cores. The orange shaded area indicates MT^2 niche. Survival time of patients (left to right): 40.4 months, 120.0 months, 9.07 months, 5.97 months. Survival status of patients (left to right): survival, survival, death, death.

(G) UMAP dimensionality reduction of SCLC macrophage subsets annotated in CosMx sequencing data. Inflam/IFN-Macro, inflammatory/interferon-primed macrophage. LA/profibrotic-Macro, lipid-associated/profibrotic macrophage. Prolif-Macro, proliferative macrophage.

(H) UMAP of SCLC macrophages showing profibrotic-associated gene signature scores.[48,53]

(I and J) Normalized pathway enrichment scores of macrophage lipid biosynthesis (I) and the ratio of exhausted T to effective T cells (J) inside and outside MT^2 niches. Paired t test. All at the core level in CosMx validation samples. Exh, exhausted; Eff, effective.

(K) GSEA plot for the top KEGG pathways correlated with macrophages inside MT2 niche. Also see Figure S8, Tables S1 and S4.
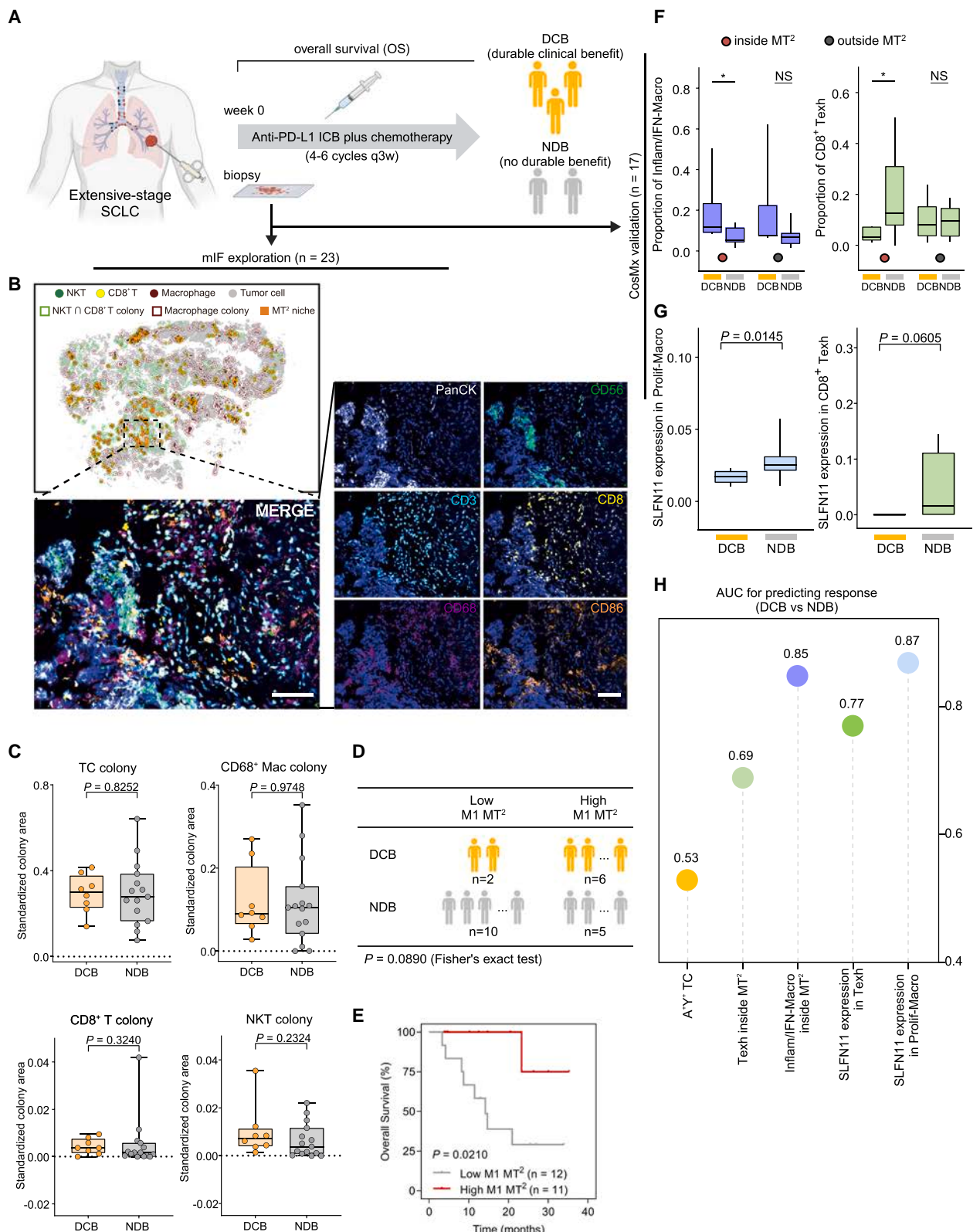
Figure 6. M1-like macrophage-based MT^2 niche predicted ICB response

(A and B) Collection of extensive-stage SCLC (ES-SCLC) patients who received anti-PD-L1 immunotherapy (A) and colony detection based on multiplex Immunofluorescence (mIF) image (B). Tissue sections were stained using antibodies against PanCK, CD3, CD8, CD56, CD68, and CD86.

(legend continued on next page)

Cancer Cell
Article

CellPress

prolonged survival following immunotherapy (Figure 6E). In contrast, the proportion of the total MT^2 area failed to predict ICB outcomes (Figure S8J).

Based on CosMx data from the ES-SCLC cohort, the cell compositions of MT^2 were correlated with the efficacy of immunotherapy (Figures 6F, and S8K and S8L). Within MT^2 niche, the proportion of M1-like Inflam/IFN-Macro was significantly higher in DCB group compared to NDB group, validating the mIF results. However, Prolif-Macro and exhausted $CD8^+$ T cells were significantly increased in NDB group. This might be associated with high SLFN11 expression (Figure 6G). Finally, we analyzed the above signatures as well as previously reported $ASCL1^+YAP1^+$ immune-hot TCs associated with ICB response,[56] and found that Inflam/IFN-Macro ratio inside MT^2 and SLFN11 expression in Prolif-Macro exhibited high performance for predicting clinical efficacy (Figure 6H).

Macrophages are recognized as functionally heterogeneous within the tumor microenvironment. Specific macrophage subsets have been shown to interact with other immune cells such as $CD8^+$ T cells, and enhance anti-tumor immunity in different cancers.[57,58] Our findings detected for the first time a stable anti-tumoral niche comprising M1-like macrophages, $CD8^+$ T cells and NKT cells, which could predict well of ICB responses in SCLC, potentially paving the way for TIME-based SCLC immunotherapies.

DISCUSSION

Multi-dimensional imaging technologies enable the capture of spatial geographical information in FFPE tissues with long-term follow-up data, supplementing the valuable studies between survival and spatial cellular analysis in SCLC. Here, we systematically produced the valuable CODEX and multi-omics data for 165 SCLC patients with long-term follow-up, based on which we reported the spatial organization of intratumoral heterogeneity and immune microenvironment at single cell level. More importantly, our proposed ColonyMap algorithm revealed a spatial-clustered immune niche (MT^2) featured as prognostic and predictive potential of informing immunotherapy response, and guiding stratified therapeutic strategies.

SCLC phenotypic heterogeneity has been increasingly recognized and delineating SCLC subtypes represent the first step toward precision medicine. In addition to the four subtypes of SCLC, single-cell resolved imaging discovered MPTCs in over 10% of TCs in this study. And neighborhood analysis enabled us to visualize the congregation of these MPTCs into unique spatial pattern within the SCLC-A subtype. The central neighborhood (CN9) was characterized by highly proliferative TCs co-expressing ASCL1 with NEUROD1 or YAP1. These observations align with emerging evidence that SCLC exhibits plasticity between distinct molecular subtypes, potentially arising from a common NE precursor cell that can dedifferentiate along divergent trajectories,[59,60] suggesting that bulk sequencing can only capture the most abundant state. Notably, our results demonstrate even a minor fraction of MPTCs within SCLC-A confers a worse prognosis, potentially attributable to their EMT phenotype. EMT provokes lack of cell-cell adhesion and enhanced migratory and therapeutic resistance, which has been increasingly implicated in SCLC pathogenesis.[10,61] The association between *RBBP6* mutations and the CN9 structure potentially mediated EMT in SCLC and promoting metastatic dissemination. Moreover, MPTCs within CN9 as well as $NEUROD1^+$ TCs within CN10 exhibited higher expression of SLFN11, a putative target of PARP inhibitors as well as an IFN-stimulated gene. Durative stimulation by TCs and inflammatory cytokines induces high SLFN11 expression in immune cells, particularly T cells, further leading to functional exhaustion and impaired immune response. Despite enhancement of spatial interactions between certain T cells in SCLC-N subtype (Figure S5H), high expression of SLFN11 may progressively remodel the immune microenvironment and ultimately lead to immunosuppression, consistent with previous report.[48] These data suggested the cellular origin, genomic alterations, and tumor cell evolutionary dynamics further shaped the SCLC subtype heterogeneity.

Moreover, the phenomenon of conspecific organisms forming colonies is widespread in the biological world. Colonies coordinate collective actions through information exchange, share resources, and enhance the adaptability and resistance of individuals.[62] Ecology research has a long history of uncovering spatial patterns in species colonies. However, the cell colony perspective has yet to be applied in spatial-omics analysis,[63] though these regions have recently been reported associating with various physiological functions and patient prognosis.[64,65] Our proposed ColonyMap algorithm provides unique advantages in studying cell aggregating patterns, colony boundaries, and colony interaction regions. Technically, the molecular and cellular tumor analysis represented the micro-scale investigations, and the tumor and organ pathological analysis represented the macro-scale research, our cell colony and CCI analysis enabled by ColonyMAP can be viewed as the meso-scale study of intratumoral structural organization.

Notably, ColonyMap can also be extended to additional spatial-omics analysis. The distinct data characteristics of spatial transcriptomics (ST) and spatial proteomics (SP) have prompted the development of specialized analytical methods to investigate cell-cell communication (CCC). The classical CCC analyses such as CellChat and CellPhoneDB are based on integrated receptor-ligand interaction data to compute intercellular communication weights and patterns, offering strong result interpretability. They mainly rely on detected gene panel,

---

(C) Comparison of TC and immune cell colony area between patients with DCB and NDB. Area of the whole slide tissue is used for standardization. Wilcoxon test. The clinical benefit was evaluated by a physician according to the response evaluation criteria in solid tumor (RECIST) v1.1.

(D) Distribution of patients with DCB and NDB between low and high M1 MT^2 abundance groups. Fisher's exact test.

(E) Kaplan-Meier curve of overall survival according to abundance of M1 MT^2 niche.

(F–H) MT^2 niche identification based on SMI CosMx sequencing in 17 ES-SCLC patients with available samples. (F) Frequency of Inflam/IFN-Macro and $CD8^+$ Texh between DCB and NDB patients inside or outside MT^2 niches. *$p < 0.5$ of t test. (G) Boxplots showing the SLFN11 expression in Prolif-Macro and $CD8^+$ Texh between DCB and NDB patients. Wilcoxon test. (H) AUC values of predictive factors in discriminating immunotherapy response in SCLC. Also see Figure S8, Tables S1 and S2.

rendering them unsuitable for technologies with limited markers. The ColonyMap algorithm, on the other hand, relies on cell type annotations and their spatial distribution patterns, making it extendable to multiple spatial platforms. Simultaneously, ColonyMap excludes discrete cells, beneficially eliminating the influence of intercellular heterogeneity. Of note, ColonyMap alone cannot elucidate the molecular mechanisms underlying colony interactions, necessitating further gene expression and pathway analyses.

Through ColonyMap, we identified the spatial distribution of the anti-tumoral MT^2 niche and revealed its positive impact on SCLC prognosis. Macrophages play a dual role in the TME,[54,66] as they can recognize, bind to, and phagocytose TCs,[67,68] but often fail to do so and can even promote tumor growth and metastasis.[69,70] Accumulating evidence suggests that macrophage-T cell cross-talk plays a pivotal role in shaping anti-tumor immunity and immunotherapy efficacy.[71,72] Tumor-infiltrated macrophages can promote T cell recruitment, activation, and effector functions through antigen presentation, cytokine secretion, and co-stimulatory signals. Conversely, activated T cells are lately reported being able to attract macrophages into their close vicinity via CCR5-signaling, and induce macrophages polarization toward an anti-tumor M1-like phenotype.[73] The ColonyMap algorithm confirmed for the first time the spatial assembly of cytotoxic T cells and macrophages in SCLC patients with favorable prognosis. Spatially, these MT^2 niches were often observed at the tumor-stroma boundary, poised to exert potential anti-tumor activity. Functionally, the macrophages within MT^2 exhibited a pro-inflammatory and high antigen-presenting phenotype, while the T cells displayed a less exhaustion state, suggesting that MT^2 assembly might enhance anti-tumor capabilities compared to dispersed immune cell types. Beyond their associations with anti-tumor immunity and patient prognosis, we further delineated the functional states of macrophages within the MT^2 niche in the immunotherapy ES-SCLC cohort, aiming to identify immune spatial structures associated with therapeutic responses. Our results demonstrated that MT^2 niches comprising pro-inflammatory M1-like macrophages correlated well with an active immune response. Studies have highlighted the critical role of multicellular structures within tumors such as CD4+CD8+APC in immunotherapeutic efficacy.[74] Specific multiple immune cell-activating antibodies (such as DC-T cell activators) have been found in murine models to possess greater anti-tumor immune capabilities than standard therapies.[75] Therefore, the MT^2 niche may also serve as an effective biomarker for clinical trial designation in SCLC, as well as potentially guiding the development of specific immune antibodies to induce immune responses in SCLC patients.

In summary, we present the first in-depth spatially resolved dataset comprised of CODEX and multi-omics information in SCLC, to our knowledge. While the previous omics studies focused on the molecular and cellular analysis of SCLC, our high-dimensional images and the developed ColonyMap informed how the tumor, blood vessel and immune cell colonies interact in space, and how the immune structural niches correlate with clinical outcomes. Given the limited therapeutic options for SCLC patients and the heterogeneous responses to immunotherapy, there is untapped translational value in exploring whether specific immune cell interactions, such as the M1-MT^2

niche, can be harnessed as prognostic and predictive factors in SCLC patients. Also, as clinical trials of advancing therapeutic strategies progress, our approach may help develop reliable guideline for SCLC patient stratification to increase therapeutic response.

Limitations of the study

Our study provides an unprecedented spatial atlas resource of SCLC and uncovers insights into its molecular heterogeneity as well as pivotal immune architectures, but there are several limitations that warrant further investigation. First, our analyses were focused on the resected limited-stage and treatment-naive SCLC. However, it remains unclear whether the spatial patterns and cellular interactions observed in this study are generalizable to metastatic tumors or patients received therapeutic drugs. Future studies incorporating a broader spectrum of SCLC stages and status will be crucial to fully elucidate the extent of spatial heterogeneity within this malignancy. Second, our spatial profiling was based on TMAs constructed from tumor tissue cores, where the TIME characteristics of individual cores might not fully represent the overall landscape of the tumor due to intra-tumoral heterogeneity. To address this, we sampled cores with a diameter of 2 mm and included two or more cores for most tumors, striking a balance between enabling high-throughput analysis and ensuring representative sampling. Finally, while our study identified potential prognostic and predictive spatial biomarkers, their clinical utility remains to be validated in prospective clinical trials. Furthermore, the development of standardized analytical pipelines and robust spatial metrics will be essential for translating these findings into clinical practice and facilitating their integration with other molecular and clinical data.

Cancer Cell
Article

CellPress

AUTHOR CONTRIBUTIONS

DECLARATION OF INTERESTS

STAR★METHODS

Detailed methods are provided in the online version of this paper and include the following:

- KEY RESOURCES TABLE
- EXPERIMENTAL MODEL AND SUBJECT DETAILS
  - Patient cohorts
  - Cell lines
  - Animals
- METHOD DETAILS
  - Construction of tissue microarray
  - CODEX antibody conjugation and panel creation
  - CODEX multiplexed imaging
  - SMI CosMx sequencing
  - Genomics and transcriptomics profiling
  - Immunohistochemistry
  - Multiplex immunofluorescence
  - Animal experiments
- QUANTIFICATION AND STATISTICAL ANALYSIS
  - CODEX image processing and single-cell segmentation
  - Single-cell lineage assignment
  - Cell-cell pairwise interaction analysis
  - Cellular neighborhood identification and Voronoi diagram generation
  - t-distributed Stochastic Neighbor Embedding (t-SNE)
  - Uniform Manifold approximation and projection (UMAP)
  - Pseudotime trajectory analysis
  - Correlation of cellular neighborhood with genomic features
  - Cell ColonyMap analysis
  - ColonyMap performance evaluation
  - Immunotherapy response evaluation
  - Survival analysis
  - Statistical analysis

SUPPLEMENTAL INFORMATION

Supplemental information can be found online at https://doi.org/10.1016/j.ccell.2025.01.012.

REFERENCES

1. George, J., Lim, J.S., Jang, S.J., Cun, Y., Ozretić, L., Kong, G., Leenders, F., Lu, X., Fernández-Cuesta, L., Bosco, G., et al. (2015). Comprehensive genomic profiles of small cell lung cancer. Nature 524, 47–53. https://doi.org/10.1038/nature14664.

2. Horn, L., Mansfield, A.S., Szczęsna, A., Havel, L., Krzakowski, M., Hochmair, M.J., Huemer, F., Losonczy, G., Johnson, M.L., Nishio, M., et al. (2018). First-Line Atezolizumab plus Chemotherapy in Extensive-Stage Small-Cell Lung Cancer. N. Engl. J. Med. 379, 2220–2229. https://doi.org/10.1056/NEJMoa1809064.

3. Cancer Genome Atlas Research Network (2014). Comprehensive molecular profiling of lung adenocarcinoma. Nature 511, 543–550. https://doi.org/10.1038/nature13385.

4. Kuang, S., and Leighl, N.B. (2021). Lorlatinib in ALK-Rearranged Lung Cancer. Cancer Cell 39, 25–27. https://doi.org/10.1016/j.ccell.2020.12.017.

5. Lin, J.J., Cardarella, S., Lydon, C.A., Dahlberg, S.E., Jackman, D.M., Jänne, P.A., and Johnson, B.E. (2016). Five-Year Survival in EGFR-Mutant Metastatic Lung Adenocarcinoma Treated with EGFR-TKIs. J. Thorac. Oncol. 11, 556–565. https://doi.org/10.1016/j.jtho.2015.12.103.

6. Ali, H.R., Rueda, O.M., Chin, S.F., Curtis, C., Dunning, M.J., Aparicio, S.A., and Caldas, C. (2014). Genome-driven integrated classification of breast cancer validated in over 7,500 samples. Genome Biol. 15, 431. https://doi.org/10.1186/s13059-014-0431-1.

7. Curtis, C., Shah, S.P., Chin, S.F., Turashvili, G., Rueda, O.M., Dunning, M.J., Speed, D., Lynch, A.G., Samarajiwa, S., Yuan, Y., et al. (2012). The genomic and transcriptomic architecture of 2,000 breast tumours reveals novel subgroups. Nature 486, 346–352. https://doi.org/10.1038/nature10983.

8. Nik-Zainal, S., Davies, H., Staaf, J., Ramakrishna, M., Glodzik, D., Zou, X., Martincorena, I., Alexandrov, L.B., Martin, S., Wedge, D.C., et al. (2016). Landscape of somatic mutations in 560 breast cancer whole-genome sequences. Nature 534, 47–54. https://doi.org/10.1038/nature17676.

9. Rudin, C.M., Poirier, J.T., Byers, L.A., Dive, C., Dowlati, A., George, J., Heymach, J.V., Johnson, J.E., Lehman, J.M., MacPherson, D., et al. (2019). Molecular subtypes of small cell lung cancer: a synthesis of human and mouse model data. Nat. Rev. Cancer 19, 289–297. https://doi.org/10.1038/s41568-019-0133-9.

10. Gay, C.M., Stewart, C.A., Park, E.M., Diao, L., Groves, S.M., Heeke, S., Nabet, B.Y., Fujimoto, J., Solis, L.M., Lu, W., et al. (2021). Patterns of transcription factor programs and immune pathway activation define four major subtypes of SCLC with distinct therapeutic vulnerabilities. Cancer Cell 39, 346–360.e7. https://doi.org/10.1016/j.ccell.2020.12.014.

11. Huang, Y.H., Klingbeil, O., He, X.Y., Wu, X.S., Arun, G., Lu, B., Somerville, T.D.D., Milazzo, J.P., Wilkinson, J.E., Demerdash, O.E., et al. (2018). POU2F3 is a master regulator of a tuft cell-like variant of small cell lung cancer. Genes Dev. 32, 915–928. https://doi.org/10.1101/gad.314815.118.

12. Liu, Q., Zhang, J., Guo, C., Wang, M., Wang, C., Yan, Y., Sun, L., Wang, D., Zhang, L., Yu, H., et al. (2024). Proteogenomic characterization of small cell lung cancer identifies biological insights and subtype-specific therapeutic strategies. Cell 187, 184–203.e28. https://doi.org/10.1016/j.cell.2023.12.004.

13. Simpson, K.L., Stoney, R., Frese, K.K., Simms, N., Rowe, W., Pearce, S.P., Humphrey, S., Booth, L., Morgan, D., Dynowski, M., et al. (2020). A biobank of small cell lung cancer CDX models elucidates inter- and intratumoral phenotypic heterogeneity. Nat. Cancer 1, 437–451. https://doi.org/10.1038/s43018-020-0046-2.

CellPress

Cancer Cell
Article

14. Ireland, A.S., Micinski, A.M., Kastner, D.W., Guo, B., Wait, S.J., Spainhower, K.B., Conley, C.C., Chen, O.S., Guthrie, M.R., Soltero, D., et al. (2020). MYC Drives Temporal Evolution of Small Cell Lung Cancer Subtypes by Reprogramming Neuroendocrine Fate. Cancer Cell 38, 60–78.e12. https://doi.org/10.1016/j.ccell.2020.05.001.

15. Goltsev, Y., Samusik, N., Kennedy-Darling, J., Bhate, S., Hale, M., Vazquez, G., Black, S., and Nolan, G.P. (2018). Deep Profiling of Mouse Splenic Architecture with CODEX Multiplexed Imaging. Cell 174, 968–981.e15. https://doi.org/10.1016/j.cell.2018.07.010.

16. Black, S., Phillips, D., Hickey, J.W., Kennedy-Darling, J., Venkataraaman, V.G., Samusik, N., Goltsev, Y., Schürch, C.M., and Nolan, G.P. (2021). CODEX multiplexed tissue imaging with DNA-conjugated antibodies. Nat. Protoc. 16, 3802–3835. https://doi.org/10.1038/s41596-021-00556-8.

17. Keren, L., Bosse, M., Marquez, D., Angoshtari, R., Jain, S., Varma, S., Yang, S.R., Kurian, A., Van Valen, D., West, R., et al. (2018). A Structured Tumor-Immune Microenvironment in Triple Negative Breast Cancer Revealed by Multiplexed Ion Beam Imaging. Cell 174, 1373–1387.e19. https://doi.org/10.1016/j.cell.2018.08.039.

18. Schurch, C.M., Bhate, S.S., Barlow, G.L., Phillips, D.J., Noti, L., Zlobec, I., Chu, P., Black, S., Demeter, J., McIlwain, D.R., et al. (2020). Coordinated Cellular Neighborhoods Orchestrate Antitumoral Immunity at the Colorectal Cancer Invasive Front. Cell 182, 1341–1359.e1319. https://doi.org/10.1016/j.cell.2020.07.005.

19. Sorin, M., Rezanejad, M., Karimi, E., Fiset, B., Desharnais, L., Perus, L.J.M., Milette, S., Yu, M.W., Maritan, S.M., Doré, S., et al. (2023). Single-cell spatial landscapes of the lung tumour immune microenvironment. Nature 614, 548–554. https://doi.org/10.1038/s41586-022-05672-3.

20. Risom, T., Glass, D.R., Averbukh, I., Liu, C.C., Baranski, A., Kagel, A., McCaffrey, E.F., Greenwald, N.F., Rivero-Gutiérrez, B., Strand, S.H., et al. (2022). Transition to invasive breast cancer is associated with progressive changes in the structure and composition of tumor stroma. Cell 185, 299–310.e18. https://doi.org/10.1016/j.cell.2021.12.023.

21. Hickey, J.W., Haist, M., Horowitz, N., Caraccio, C., Tan, Y., Rech, A.J., Baertsch, M.A., Rovira-Clavé, X., Zhu, B., Vazquez, G., et al. (2023). T cell-mediated curation and restructuring of tumor tissue coordinates an effective immune response. Cell Rep. 42, 113494. https://doi.org/10.1016/j.celrep.2023.113494.

22. Pietanza, M.C., Waqar, S.N., Krug, L.M., Dowlati, A., Hann, C.L., Chiappori, A., Owonikoko, T.K., Woo, K.M., Cardnell, R.J., Fujimoto, J., et al. (2018). Randomized, Double-Blind, Phase II Study of Temozolomide in Combination With Either Veliparib or Placebo in Patients With Relapsed-Sensitive or Refractory Small-Cell Lung Cancer. J. Clin. Oncol. 36, 2386–2394. https://doi.org/10.1200/JCO.2018.77.7672.

23. Paz-Ares, L., Champiat, S., Lai, W.V., Izumi, H., Govindan, R., Boyer, M., Hummel, H.D., Borghaei, H., Johnson, M.L., Steeghs, N., et al. (2023). Tarlatamab, a First-in-Class DLL3-Targeted Bispecific T-Cell Engager, in Recurrent Small-Cell Lung Cancer: An Open-Label, Phase I Study. J. Clin. Oncol. 41, 2893–2903. https://doi.org/10.1200/JCO.22.02823.

24. Hellmann, M.D., Callahan, M.K., Awad, M.M., Calvo, E., Ascierto, P.A., Atmaca, A., Rizvi, N.A., Hirsch, F.R., Selvaggi, G., Szustakowski, J.D., et al. (2018). Tumor Mutational Burden and Efficacy of Nivolumab Monotherapy and in Combination with Ipilimumab in Small-Cell Lung Cancer. Cancer Cell 33, 853–861.e4. https://doi.org/10.1016/j.ccell.2018.04.001.

25. Liu, S.V., Reck, M., Mansfield, A.S., Mok, T., Scherpereel, A., Reinmuth, N., Garassino, M.C., De Castro Carpeno, J., Califano, R., Nishio, M., et al. (2021). Updated Overall Survival and PD-L1 Subgroup Analysis of Patients With Extensive-Stage Small-Cell Lung Cancer Treated With Atezolizumab, Carboplatin, and Etoposide (IMpower133). J. Clin. Oncol. 39, 619–630. https://doi.org/10.1200/JCO.20.01055.

26. Qu, S., Fetsch, P., Thomas, A., Pommier, Y., Schrump, D.S., Miettinen, M.M., and Chen, H. (2022). Molecular Subtypes of Primary SCLC Tumors and Their Associations With Neuroendocrine and Therapeutic Markers. J. Thorac. Oncol. 17, 141–153. https://doi.org/10.1016/j.jtho.2021.08.763.

27. Baine, M.K., Hsieh, M.S., Lai, W.V., Egger, J.V., Jungbluth, A.A., Daneshbod, Y., Beras, A., Spencer, R., Lopardo, J., Bodd, F., et al. (2020). SCLC Subtypes Defined by ASCL1, NEUROD1, POU2F3, and YAP1: A Comprehensive Immunohistochemical and Histopathologic Characterization. J. Thorac. Oncol. 15, 1823–1835. https://doi.org/10.1016/j.jtho.2020.09.009.

28. Deng, C., Wang, Y., Fu, F., Li, D., Zheng, Q., Jin, Y., Li, Y., Chen, H., and Zhang, Y. (2023). Tumor-derived Vimentin as a novel biomarker for distinct subtypes predicting adjuvant chemotherapy resistance and T-cell-inflamed phenotype in small cell lung cancer. MedComm 4, e370. https://doi.org/10.1002/mco2.370.

29. Baine, M.K., Febres-Aldana, C.A., Chang, J.C., Jungbluth, A.A., Sethi, S., Antonescu, C.R., Travis, W.D., Hsieh, M.S., Roh, M.S., Homer, R.J., et al. (2022). POU2F3 in SCLC: Clinicopathologic and Genomic Analysis With a Focus on Its Diagnostic Utility in Neuroendocrine-Low SCLC. J. Thorac. Oncol. 17, 1109–1121. https://doi.org/10.1016/j.jtho.2022.06.004.

30. Virassamy, B., Caramia, F., Savas, P., Sant, S., Wang, J., Christo, S.N., Byrne, A., Clarke, K., Brown, E., Teo, Z.L., et al. (2023). Intratumoral CD8(+) T cells with a tissue-resident memory phenotype mediate local immunity and immune checkpoint responses in breast cancer. Cancer Cell 41, 585–601.e8. https://doi.org/10.1016/j.ccell.2023.01.004.

31. van der Leun, A.M., Thommen, D.S., and Schumacher, T.N. (2020). CD8(+) T cell states in human cancer: insights from single-cell analysis. Nat. Rev. Cancer 20, 218–232. https://doi.org/10.1038/s41568-019-0235-4.

32. Sun, P., He, J., Chao, X., Chen, K., Xu, Y., Huang, Q., Yun, J., Li, M., Luo, R., Kuang, J., et al. (2021). A Computational Tumor-Infiltrating Lymphocyte Assessment Method Comparable with Visual Reporting Guidelines for Triple-Negative Breast Cancer. EBioMedicine 70, 103492. https://doi.org/10.1016/j.ebiom.2021.103492.

33. Federico, L., McGrail, D.J., Bentebibel, S.E., Haymaker, C., Ravelli, A., Forget, M.A., Karpinets, T., Jiang, P., Reuben, A., Negrao, M.V., et al. (2022). Distinct tumor-infiltrating lymphocyte landscapes are associated with clinical outcomes in localized non-small-cell lung cancer. Ann. Oncol. 33, 42–56. https://doi.org/10.1016/j.annonc.2021.09.021.

34. Jackson, H.W., Fischer, J.R., Zanotelli, V.R.T., Ali, H.R., Mechera, R., Soysal, S.D., Moch, H., Muenst, S., Varga, Z., Weber, W.P., and Bodenmiller, B. (2020). The single-cell pathology landscape of breast cancer. Nature 578, 615–620. https://doi.org/10.1038/s41586-019-1876-x.

35. Xiong, J., Barayan, R., Louie, A.V., and Lok, B.H. (2022). Novel therapeutic combinations with PARP inhibitors for small cell lung cancer: A bench-to-bedside review. Semin. Cancer Biol. 86, 521–542. https://doi.org/10.1016/j.semcancer.2022.07.008.

36. Murai, J., Thomas, A., Miettinen, M., and Pommier, Y. (2019). Schlafen 11 (SLFN11), a restriction factor for replicative stress induced by DNA-targeting anti-cancer therapies. Pharmacol. Ther. 201, 94–102. https://doi.org/10.1016/j.pharmthera.2019.05.009.

37. Murai, J., Tang, S.W., Leo, E., Baechler, S.A., Redon, C.E., Zhang, H., Al Abo, M., Rajapakse, V.N., Nakamura, E., Jenkins, L.M.M., et al. (2018). SLFN11 Blocks Stressed Replication Forks Independently of ATR. Mol. Cell 69, 371–384.e6. https://doi.org/10.1016/j.molcel.2018.01.012.

38. Moore, K., Colombo, N., Scambia, G., Kim, B.G., Oaknin, A., Friedlander, M., Lisyanskaya, A., Floquet, A., Leary, A., Sonke, G.S., et al. (2018). Maintenance Olaparib in Patients with Newly Diagnosed Advanced Ovarian Cancer. N. Engl. J. Med. 379, 2495–2505. https://doi.org/10.1056/NEJMoa1810858.

39. Davies, H., Glodzik, D., Morganella, S., Yates, L.R., Staaf, J., Zou, X., Ramakrishna, M., Martin, S., Boyault, S., Sieuwerts, A.M., et al. (2017). HRDetect is a predictor of BRCA1 and BRCA2 deficiency based on mutational signatures. Nat. Med. 23, 517–525. https://doi.org/10.1038/nm.4292.

40. Jonsson, P., Bandlamudi, C., Cheng, M.L., Srinivasan, P., Chavan, S.S., Friedman, N.D., Rosen, E.Y., Richards, A.L., Bouvier, N., Selcuklu, S.D.,

Cancer Cell
Article

CellPress

et al. (2019). Tumour lineage shapes BRCA-mediated phenotypes. Nature *571*, 576–579. https://doi.org/10.1038/s41586-019-1382-1.

41. Sade-Feldman, M., Jiao, Y.J., Chen, J.H., Rooney, M.S., Barzily-Rokni, M., Eliane, J.P., Bjorgaard, S.L., Hammond, M.R., Vitzthum, H., Blackmon, S.M., et al. (2017). Resistance to checkpoint blockade therapy through inactivation of antigen presentation. Nat. Commun. *8*, 1136. https://doi.org/10.1038/s41467-017-01062-w.

42. Rooney, M.S., Shukla, S.A., Wu, C.J., Getz, G., and Hacohen, N. (2015). Molecular and genetic properties of tumors associated with local immune cytolytic activity. Cell *160*, 48–61. https://doi.org/10.1016/j.cell.2014.12.033.

43. Xiao, C., Wu, G., Zhou, Z., Zhang, X., Wang, Y., Song, G., Ding, E., Sun, X., Zhong, L., Li, S., et al. (2019). RBBP6, a RING finger-domain E3 ubiquitin ligase, induces epithelial-mesenchymal transition and promotes metastasis of colorectal cancer. Cell Death Dis. *10*, 833. https://doi.org/10.1038/s41419-019-2070-7.

44. George, J., Maas, L., Abedpour, N., Cartolano, M., Kaiser, L., Fischer, R.N., Scheel, A.H., Weber, J.P., Hellmich, M., Bosco, G., et al. (2024). Evolutionary trajectories of small cell lung cancer under therapy. Nature *627*, 880–889. https://doi.org/10.1038/s41586-024-07177-7.

45. Shen, J.Z., Qiu, Z., Wu, Q., Zhang, G., Harris, R., Sun, D., Rantala, J., Barshop, W.D., Zhao, L., Lv, D., et al. (2022). A FBXO7/EYA2-SCF(FBXW7) axis promotes AXL-mediated maintenance of mesenchymal and immune evasion phenotypes of cancer cells. Mol. Cell *82*, 1123–1139.e8. https://doi.org/10.1016/j.molcel.2022.01.022.

46. Wolin, A.R., Vincent, M.Y., Hotz, T., Purdy, S.C., Rosenbaum, S.R., Hughes, C.J., Hsu, J.Y., Oliphant, M.U.J., Armstrong, B., Wessells, V., et al. (2023). EYA2 tyrosine phosphatase inhibition reduces MYC and prevents medulloblastoma progression. Neuro Oncol. *25*, 2287–2301. https://doi.org/10.1093/neuonc/noad128.

47. Ntwasa, M. (2016). Retinoblastoma Binding Protein 6, Another p53 Monitor. Trends Cancer *2*, 635–637. https://doi.org/10.1016/j.trecan.2016.10.003.

48. Chan, J.M., Quintanal-Villalonga, Á., Gao, V.R., Xie, Y., Allaj, V., Chaudhary, O., Masilionis, I., Egger, J., Chow, A., Walle, T., et al. (2021). Signatures of plasticity, metastasis, and immunosuppression in an atlas of human small cell lung cancer. Cancer Cell *39*, 1479–1496.e18. https://doi.org/10.1016/j.ccell.2021.09.008.

49. Chousakos, E., Kose, K., Kurtansky, N.R., Dusza, S.W., Halpern, A.C., and Marghoob, A.A. (2022). Analyzing the Spatial Randomness in the Distribution of Acquired Melanocytic Neoplasms. J. Invest. Dermatol. *142*, 3274–3281. https://doi.org/10.1016/j.jid.2022.06.011.

50. Zhang, P., Hu, X., Li, Z., Liu, Q., Liu, L., Jin, Y., Liu, S., Zhao, X., Wang, J., Hao, D., et al. (2024). Schlafen 11 triggers innate immune responses through its ribonuclease activity upon detection of single-stranded DNA. Sci. Immunol. *9*, eadj5465. https://doi.org/10.1126/sciimmunol.adj5465.

51. Allison Stewart, C., Tong, P., Cardnell, R.J., Sen, T., Li, L., Gay, C.M., Masrorpour, F., Fan, Y., Bara, R.O., Feng, Y., et al. (2017). Dynamic variations in epithelial-to-mesenchymal transition (EMT), ATM, and SLFN11 govern response to PARP inhibitors and cisplatin in small cell lung cancer. Oncotarget *8*, 28575–28587. https://doi.org/10.18632/oncotarget.15338.

52. Seaman, S., Zhu, Z., Saha, S., Zhang, X.M., Yang, M.Y., Hilton, M.B., Morris, K., Szot, C., Morris, H., Swing, D.A., et al. (2017). Eradication of Tumors through Simultaneous Ablation of CD276/B7-H3-Positive Tumor Cells and Tumor Vasculature. Cancer Cell *31*, 501–515.e8. https://doi.org/10.1016/j.ccell.2017.03.005.

53. Adams, T.S., Schupp, J.C., Poli, S., Ayaub, E.A., Neumark, N., Ahangari, F., Chu, S.G., Raby, B.A., DeIuliis, G., Januszyk, M., et al. (2020). Single-cell RNA-seq reveals ectopic and aberrant lung-resident cell populations in idiopathic pulmonary fibrosis. Sci. Adv. *6*, eaba1983. https://doi.org/10.1126/sciadv.aba1983.

54. Ma, R.Y., Black, A., and Qian, B.Z. (2022). Macrophage diversity in cancer revisited in the era of single-cell omics. Trends Immunol. *43*, 546–563. https://doi.org/10.1016/j.it.2022.04.008.

55. Liu, B., Zhang, Y., Wang, D., Hu, X., and Zhang, Z. (2022). Single-cell meta-analyses reveal responses of tumor-reactive CXCL13(+) T cells to immune-checkpoint blockade. Nat. Cancer *3*, 1123–1136. https://doi.org/10.1038/s43018-022-00433-7.

56. Nabet, B.Y., Hamidi, H., Lee, M.C., Banchereau, R., Morris, S., Adler, L., Gayevskiy, V., Elhossiny, A.M., Srivastava, M.K., Patil, N.S., et al. (2024). Immune heterogeneity in small-cell lung cancer and vulnerability to immune checkpoint blockade. Cancer Cell *42*, 429–443.e4. https://doi.org/10.1016/j.ccell.2024.01.010.

57. Nalio Ramos, R., Missolo-Koussou, Y., Gerber-Ferder, Y., Bromley, C.P., Bugatti, M., Núñez, N.G., Tosello Boari, J., Richer, W., Menger, L., Denizeau, J., et al. (2022). Tissue-resident FOLR2(+) macrophages associate with CD8(+) T cell infiltration in human breast cancer. Cell *185*, 1189–1207.e25. https://doi.org/10.1016/j.cell.2022.02.021.

58. Bugatti, M., Bergamini, M., Missale, F., Monti, M., Ardighieri, L., Pezzali, I., Picinoli, S., Caronni, N., Missolo-Koussou, Y., Helft, J., et al. (2022). A Population of TIM4+FOLR2+ Macrophages Localized in Tertiary Lymphoid Structures Correlates to an Active Immune Infiltrate Across Several Cancer Types. Cancer Immunol. Res. *10*, 1340–1353. https://doi.org/10.1158/2326-6066.CIR-22-0271.

59. Oser, M.G., Sabet, A.H., Gao, W., Chakraborty, A.A., Schinzel, A.C., Jennings, R.B., Fonseca, R., Bonal, D.M., Booker, M.A., Flaifel, A., et al. (2019). The KDM5A/RBP2 histone demethylase represses NOTCH signaling to sustain neuroendocrine differentiation and promote small cell lung cancer tumorigenesis. Genes Dev. *33*, 1718–1738. https://doi.org/10.1101/gad.328336.119.

60. Razavi, P., Li, B.T., Brown, D.N., Jung, B., Hubbell, E., Shen, R., Abida, W., Juluru, K., De Bruijn, I., Hou, C., et al. (2019). High-intensity sequencing reveals the sources of plasma circulating cell-free DNA variants. Nat. Med. *25*, 1928–1937. https://doi.org/10.1038/s41591-019-0652-7.

61. Stewart, C.A., Gay, C.M., Xi, Y., Sivajothi, S., Sivakamasundari, V., Fujimoto, J., Bolisetty, M., Hartsfield, P.M., Balasubramaniyan, V., Chalishazar, M.D., et al. (2020). Single-cell analyses reveal increased intratumoral heterogeneity after the onset of therapy resistance in small-cell lung cancer. Nat. Cancer *1*, 423–436. https://doi.org/10.1038/s43018-019-0020-z.

62. Winston, J.E. (2010). Life in the colonies: learning the alien ways of colonial organisms. Integr. Comp. Biol. *50*, 919–933. https://doi.org/10.1093/icb/icq146.

63. de Souza, N., Zhao, S., and Bodenmiller, B. (2024). Multiplex protein imaging in tumour biology. Nat. Rev. Cancer *24*, 171–191. https://doi.org/10.1038/s41568-023-00657-4.

64. Xun, Z., Ding, X., Zhang, Y., Zhang, B., Lai, S., Zou, D., Zheng, J., Chen, G., Su, B., Han, L., and Ye, Y. (2023). Reconstruction of the tumor spatial microenvironment along the malignant-boundary-nonmalignant axis. Nat. Commun. *14*, 933. https://doi.org/10.1038/s41467-023-36560-7.

65. Fridman, W.H., Meylan, M., Petitprez, F., Sun, C.M., Italiano, A., and Sautès-Fridman, C. (2022). B cells and tertiary lymphoid structures as determinants of tumour immune contexture and clinical outcome. Nat. Rev. Clin. Oncol. *19*, 441–457. https://doi.org/10.1038/s41571-022-00619-z.

66. Qian, B.Z., and Pollard, J.W. (2010). Macrophage diversity enhances tumor progression and metastasis. Cell *141*, 39–51. https://doi.org/10.1016/j.cell.2010.03.014.

67. Gul, N., Babes, L., Siegmund, K., Korthouwer, R., Bogels, M., Braster, R., Vidarsson, G., ten Hagen, T.L., Kubes, P., and van Egmond, M. (2014). Macrophages eliminate circulating tumor cells after monoclonal antibody therapy. J. Clin. Investig. *124*, 812–823. https://doi.org/10.1172/JCI66776.

68. Chao, M.P., Jaiswal, S., Weissman-Tsukamoto, R., Alizadeh, A.A., Gentles, A.J., Volkmer, J., Weiskopf, K., Willingham, S.B., Raveh, T., Park, C.Y., et al. (2010). Calreticulin is the dominant pro-phagocytic signal on multiple human cancers and is counterbalanced by CD47. Sci. Transl. Med. *2*, 63ra94. https://doi.org/10.1126/scitranslmed.3001375.

69. De Palma, M., and Lewis, C.E. (2013). Macrophage regulation of tumor responses to anticancer therapies. Cancer Cell *23*, 277–286. https://doi.org/10.1016/j.ccr.2013.02.013.

70. Cassetta, L., and Pollard, J.W. (2018). Targeting macrophages: therapeutic approaches in cancer. Nat. Rev. Drug Discov. *17*, 887–904. https://doi.org/10.1038/nrd.2018.169.

71. Bonavita, E., Bromley, C.P., Jonsson, G., Pelly, V.S., Sahoo, S., Walwyn-Brown, K., Mensurado, S., Moeini, A., Flanagan, E., Bell, C.R., et al. (2020). Antagonistic Inflammatory Phenotypes Dictate Tumor Fate and Response to Immune Checkpoint Blockade. Immunity *53*, 1215–1229.e8. https://doi.org/10.1016/j.immuni.2020.10.020.

72. Klug, F., Prakash, H., Huber, P.E., Seibel, T., Bender, N., Halama, N., Pfirschke, C., Voss, R.H., Timke, C., Umansky, L., et al. (2013). Low-dose irradiation programs macrophage differentiation to an iNOS(+)/M1 phenotype that orchestrates effective T cell immunotherapy. Cancer Cell *24*, 589–602. https://doi.org/10.1016/j.ccr.2013.09.014.

73. van Elsas, M.J., Middelburg, J., Labrie, C., Roelands, J., Schaap, G., Sluijter, M., Tonea, R., Ovcinnikovs, V., Lloyd, K., Schuurman, J., et al. (2024). Immunotherapy-activated T cells recruit and skew late-stage activated M1-like macrophages that are critical for therapeutic efficacy. Cancer Cell *42*, 1032–1050.e10. https://doi.org/10.1016/j.ccell.2024.04.011.

74. Espinosa-Carrasco, G., Chiu, E., Scrivo, A., Zumbo, P., Dave, A., Betel, D., Kang, S.W., Jang, H.J., Hellmann, M.D., Burt, B.M., et al. (2024). Intratumoral immune triads are required for immunotherapy-mediated elimination of solid tumors. Cancer Cell *42*, 1202–1216.e8. https://doi.org/10.1016/j.ccell.2024.05.025.

75. Shapir Itai, Y., Barboy, O., Salomon, R., Bercovich, A., Xie, K., Winter, E., Shami, T., Porat, Z., Erez, N., Tanay, A., et al. (2024). Bispecific dendritic-T cell engager potentiates anti-tumor immunity. Cell *187*, 375–389.e18. https://doi.org/10.1016/j.cell.2023.12.011.

76. Bankhead, P., Loughrey, M.B., Fernández, J.A., Dombrowski, Y., McArt, D.G., Dunne, P.D., McQuaid, S., Gray, R.T., Murray, L.J., Coleman, H.G., et al. (2017). QuPath: Open source software for digital pathology image analysis. Sci. Rep. *7*, 16878. https://doi.org/10.1038/s41598-017-17204-5.

77. Schapiro, D., Jackson, H.W., Raghuraman, S., Fischer, J.R., Zanotelli, V.R.T., Schulz, D., Giesen, C., Catena, R., Varga, Z., and Bodenmiller, B. (2017). histoCAT: analysis of cell phenotypes and interactions in multiplex image cytometry data. Nat. Methods *14*, 873–876. https://doi.org/10.1038/nmeth.4391.

78. Sondka, Z., Bamford, S., Cole, C.G., Ward, S.A., Dunham, I., and Forbes, S.A. (2018). The COSMIC Cancer Gene Census: describing genetic dysfunction across all human cancers. Nat. Rev. Cancer *18*, 696–705. https://doi.org/10.1038/s41568-018-0060-1.

Cancer Cell
Article

⤭ CellPress

STAR★METHODS

KEY RESOURCES TABLE

REAGENT or RESOURCE	SOURCE	IDENTIFIER
Antibodies		
A full list of antibodies is provided in Table S2	N/A	N/A
Biological samples		
FFPE of 144 limited-stage SCLC patients	Fudan University Shanghai Cancer Center	This paper
CODEX TMAs of limited-stage 129 SCLC patients	Fudan University Shanghai Cancer Center	This paper
Paired tumor and normal adjacent lung tissues of 109 limited-stage SCLC patients	Fudan University Shanghai Cancer Center	This paper
Biopsy samples of an independent cohort of 23 extensive-stage SCLC patients	Fudan University Shanghai Cancer Center	This paper
Chemicals, peptides, and recombinant proteins		
TBS IHC Wash Buffer with Tween 20	Cell Marque	Cat#935B-09
IHC Detect Kit for Rabbit/Mouse Primary Antibody	Proteintech	Cat#PK10006
TSA 7-color kit	Absinbio	Cat#50037-100T
Anti-Rabbit/Mouse Immunoglobulins/HRP	Absinbio	Cat#50015-02
QIAamp DNA tissue kit	QIAGEN	Cat#51404
AmoyDx RNA Extraction Kits	Amoy Diagnostics	Cat#FF03
Ribo-Zero gold rRNA removal kit	Illumina	Cat#MRZG126
NEBNext® Magnesium RNA Fragmentation Module	New England Biolabs	Cat#E6150S
Critical commercial assays		
10X Buffer Kit for PhenoCycler-Fusion (Formerly CODEX)	Akoya Biosciences	Cat#7000019
Assay Reagent for PhenoCycler (1.25 mL)	Akoya Biosciences	Cat#7000002
Flow Cell 2PK for PhenoCycler-Fusion	Akoya Biosciences	Cat#240204
Nuclear Stain for PhenoCycler (1 mL)	Akoya Biosciences	Cat#7000003
96 well plates for PhenoCycler	Akoya Biosciences	Cat#7000006
96 well plate seals for PhenoCycler	Akoya Biosciences	Cat#7000007
Staining Kit for PhenoCycler (10 test)	Akoya Biosciences	Cat#7000008
Deposited data		
Processed primary imaging data	This paper	https://zenodo.org/records/11115430
SCLC scRNA-seq	Chan et al.[48]	https://cellxgene.cziscience.com/collections/62e8f058-9c37-48bc-9200-e767f318a8ec
WES and RNA-seq data	This paper	GSA database: HRA007321 for WES; HRA007339 for RNA-seq
Experimental Models: Cell Lines		
Human: H69 cells	ATCC	Cat#HTB-119
Experimental models: Organisms/strains		
Mouse: BALB/c nude, male	LC Company, Shanghai	N/A
Software and algorithms		
Data analysis was done using R 4.3.1	R	N/A
Data analysis was done using Python 3.11.5	Python	N/A
All analysis code is available at code repository:	This paper	https://github.com/wangjun-hub/CODEX_SCLC

EXPERIMENTAL MODEL AND SUBJECT DETAILS

Patient cohorts

We utilized a prospective limited-stage surgically resected SCLC cohort of patients from Fudan University Human Lung Tissue Multi-omics Atlas (HLTMA). This cohort included 165 primary resected SCLC patients diagnosed between 2010 and 2021, with available tissues for immunohistochemistry ($n = 144$), CODEX ($n = 129$), bulk RNA sequencing ($n = 109$), whole-exome sequencing ($n = 87$), and SMI CosMx ($n = 50$). Another extensive-stage immunotherapy SCLC cohort ($n = 23$) who received PD-L1 blockade combined with chemotherapy [atezolizumab 1,200 mg every three weeks (q3w) or durvalumab 1,500 mg q3w] was collected for multiplex Immuno-fluorescence (mIF) and CosMx validation and exploration for immunotherapy response prediction. This study was approved by the Fudan University Shanghai Cancer Center (FUSCC) Institutional Review Board (IRB#2111246-9) and written informed consents of all participating patients were obtained. Clinicopathological information on two cohorts included can be found in Table S1.

Cell lines

Human H69 cells were generously provided by Prof. Zhiwen Zhang at Fudan University. All the human SCLC cells were cultured in RPMI 1640 medium with 10% FBS, penicillin and streptomycin.

Animals

Four-week-old male BALB/c nude mice were purchased from LC Company (Shanghai, China) and used for establishment of lung orthotopic SCLC cell line models. We used an optimized environment to house the mice, including a 12/12-h light/dark cycle, 20°C–23°C temperatures with 40–60% humidity, and standard diet/water. All animal experiments were conducted following a protocol approved by the Institutional Animal Care and Use Committee of FUSCC.

METHOD DETAILS

Construction of tissue microarray

Areas of carcinoma suitable for staining were identified on H&E stained slides by a thorax pathologist (Q.Z.). And tissue Microarray (TMA) blocks with 251 2.0-mm tumor cores were generated by removing and processing the marked regions. Additional 16 adjacent normal region cores were extracted from paired normal tissue blocks. Of the 129 tumors included in this analysis, 118 were represented by two cores, nine were represented by one core and two were represented by three cores. Where tumors were represented by more than one core, data from all cores were used to compute cell numbers and cell phenotype proportions per patient. We used the subset of tumors represented by two cores to assess the spatial intratumoral heterogeneity (Figure S2). Sections of TMA slides were cut onto glass slides for CODEX, CosMx and H&E staining.

CODEX antibody conjugation and panel creation

CODEX multiplexed imaging was performed according to the CODEX staining and imaging protocol previously described.[16] Antibody panels were carefully curated to include targets that identify subtypes of tumor, stromal, innate, and adaptive immune cells, as well as cell functional markers (Table S2). Each antibody was conjugated to a unique oligonucleotide barcode, and tissues were stained with these antibody-oligonucleotide conjugates. Staining patterns were validated against established immunohisto-chemistry profiles in positive control intestinal or tonsillar tissues. Concurrently, H&E morphological staining confirmed the localization of marker expression. Prior to multiplexed CODEX cycles, antibody-oligonucleotide conjugates underwent low-plex fluorescence assays to evaluate signal-to-noise ratios and optimize staining conditions. Subsequently, the entire validated antibody panel was employed in a single, highly multiplexed CODEX experiment.

CODEX multiplexed imaging

Upon validating the curated antibody-oligonucleotide conjugate panel, we performed multiplexed CODEX imaging on tissue arrays. This cyclical process involved sequential stripping, annealing, and imaging of fluorescently labeled oligonucleotides complementary to the oligonucleotide barcodes on the conjugates. Prior to full-scale CODEX multiplexing, a test run was conducted to further optimize signal-to-noise ratios, antibody dilutions, exposure times, and appropriate cycling for each conjugate. Ultimately, the tissue arrays underwent comprehensive multiplexed CODEX imaging, with metadata from each run provided in Table S1.

SMI CosMx sequencing

The Spatial Molecular Imager (SMI) CosMx Sequencing technology represents a powerful approach for *in situ* transcriptomics and proteomics analysis at subcellular resolution. This enzyme-free, amplification-free, hybridization-based single-molecule barcoding methodology enables the direct interrogation of intact FFPE samples on standard pathology glass slides. The SMI approach employs a two-component probe design, consisting of a target-binding domain and a readout domain. The target-binding domain is a 35-to-50 nucleotide sequence that hybridizes to the target RNA of interest, while the readout domain contains four consecutive 10-to-20 nucleotide reporter-landing sequences. These landing sequences are subsequently hybridized with fluorescently labeled branched reporters, enabling a 64-bit barcoding scheme through combinatorial signaling across four fluorescent channels.

Cancer Cell
Article

The SMI CosMx sequencing workflow involves standard tissue preparation, followed by probe hybridization and cyclic reporter readout within a flow cell integrated with the SMI instrument. Notably, our implementation utilizes a gene panel encompassing 6,000 targets, enabling comprehensive transcriptomic profiling. Following each round of reporter hybridization and imaging, a UV cleavage step efficiently quenches the fluorescent signals, allowing for the subsequent incubation with the next set of reporters.

Genomics and transcriptomics profiling

The total DNA was extracted from tissues using QIAamp DNA tissue kit (QIAGEN) according to the manufacturer's protocol. To construct sequencing library, DNA was fragmented using Covaris M220 focused-ultrasonicator (Covaris). Then, exome was captured using the Human Exome 2.0 Plus (Twist Bioscience) according to the vendor's protocol. The final DNA library with 150 bp paired-end reads was sequenced on the Illumina Novaseq 6000 platform (Illumina).

Total RNA was extracted using AmoyDx RNA kit (Amoy Diagnostics) and quality-checked with the Agilent Bioanalyzer 2100 system (Agilent Technologies). Samples with RNA integrity number (RIN) > 7.0 were considered high quality. Ribosomal RNA was depleted from 5 μg total RNA using the Ribo-Zero gold rRNA removal kit (Illumina), followed by fragmentation into short segments (NEBNext Magnesium RNA Fragmentation Module). Finally, paired-end (2 x 150 bp) sequencing was performed on the Illumina NovaSeq 6000 platform following the manufacturer's protocol.

Immunohistochemistry

TMAs and slides were stained for subtype-defined markers of SCLC including ASCL1 (Abcam), NEUROD1 (Abcam), POU2F3 (Santa Cruz) and YAP1 (Santa Cruz) using Anti-mouse/rabbit Immunohistochemistry (IHC) Detection Kit (Proteintech) according to the manufacture protocol. Two independent pathologists (Y.L. and Q.Z.) reviewed the stained slides in a blinded fashion. For the IHC-based molecular subtyping for SCLC samples, we adopted the common histscore (H-score, range 0–300) method, which was calculated by multiplying the proportion of marker-positive TCs (0%–100%) by the intensity of positive staining (no staining = 0, weak staining = 1, moderate staining = 2, and strong staining = 3). And the final tumor subtype was assigned based on the highest H-score among subtyping markers.

Multiplex immunofluorescence

FFPE whole tissue sections were stained using antibodies against cytokeratins (Absinbio), CD3 (Absinbio), CD8 (Absinbio), CD56 (Absinbio), CD68 (Absinbio) and CD86 (Absinbio). All antibodies were linked with one of the fluorophores from the TSA 7-color kit (Absinbio) following the manufacturer's protocol. Sections were scanned by a tissue imaging system (Aperio Versa 8; Leica).

Animal experiments

Establishment of an orthotopic lung cancer model was achieved through intrapulmonary injection in 4-week-old male nude mice. Mice were anesthetized with pentobarbital (50 mg/kg sodium) and positioned in right lateral decubitus. Following an 8–10 mm incision in the left thoracic wall, the pleural cavity was exposed, providing visualization of the left lung. A cell suspension comprising 1 × 10^6 H69 cells, exhibiting greater than 90% viability, was prepared in 40 μL PBS supplemented with 40 μg growth factor-reduced Matrigel. The suspension was directly inoculated into the left lung parenchyma via the pleural. Post-injection, the surgical site was stapled, and mice were positioned in left lateral decubitus for recovery monitoring until fully recovered.

Four weeks post-implantation of the orthotopic lung tumor model, mice underwent multiparametric magnetic resonance imaging (MRI) to evaluate primary tumor establishment and metastatic dissemination. MRI was performed on a 7T small animal MRI system (Bruker BioSpin, Billerica, MA) and T2-weighted images of the brain, lungs, and abdomen were acquired. Mice bearing orthotopic lung tumors were euthanized, and their lungs were resected and subjected to an enzymatic digestion protocol adapted from published methods. Single-cell capture, barcoding, and library preparation were performed using the 10x Genomics Chromium Next GEM Single Cell 3′ v3.1 platform according to the manufacturer's instructions. Final libraries were sequenced on the Illumina NovaSeq 6000 system using 150bp paired-end sequencing.

QUANTIFICATION AND STATISTICAL ANALYSIS

CODEX image processing and single-cell segmentation

After completing the CODEX and mIF staining experiment, each raw QPTIFF images were imported into QuPath (version 0.3.2)[76] for initial quality control, including image stitching, drift compensation, deconvolution, and cycle concatenation. Artifacts such as out-of-focus regions, tissue folding, and debris were manually annotated and excluded from the analysis. Individual cell segmentation was performed to obtain quantitative single cell information. Processed images were then segmented using deep-learning based algorithm StarDist, utilizing its default parameters, and applying the model to the DAPI channel. To enhance image contrast for prediction, preprocessing steps were implemented, including reducing the image size by 50% and applying contrast limited adaptive histogram equalization. The centroid of each cell was subsequently determined using the x-y coordinates. A comprehensive qualitative assessment of the segmentation was carried out by two specialized pathologists (Y.L. and Q.Z.) to affirm the robustness and reliability of the segmentation process. Both the QuPath software and StarDist script can be downloaded at https://github.com/qupath/qupath/releases and https://github.com/qupath/qupath-extension-stardist/releases.

Single-cell lineage assignment

The average intensity of each protein marker was then calculated for individual cell object using the segmentation masks and normalized by object area. Owing to existing phenotyping challenges for highly multiplexed imaging, we created a cell phenotyping pipeline based on canonical lineage markers and used a supervised hierarchal approach to assign cell phenotypes (Figure S1C). Considered that using thresholding as a single measurement for cell phenotyping might not sufficient to generate a usable classification, we selected a machine learning-based cell annotation method available in QuPath to train image classifiers and perform cell phenotyping. This approach allows for the integration of mutually exclusive markers (i.e., lineage markers) within a single classifier and facilitates training on duplicate image sets. By manually annotating positive and negative cells based on fluorescence expression patterns (a process supervised by pathologists), the model integrated cell phenotypes across classifiers and applied the trained parameters to entire images. The resulting cell annotations were re-validated by pathologists, and inaccuracies were addressed by increasing the training dataset (object counts) and adjusting types of training cells. For functional markers beyond lineage markers, such as immune checkpoints PD-1, PD-L1, or potential SCLC targets DDL3, SLFN11, we employed the same methodology to train individual classifier for each marker. Positive cells were identified, and their proportions within interesting cell populations were quantified, enabling the assessment of functional phenotypic heterogeneity.

Cell-cell pairwise interaction analysis

We performed a permutation-test-based single-cell pairwise interaction analysis[77] which detected cell phenotype pairs that show stronger ("interaction") or weaker ("avoidance") co-localization compared with a random distribution derived by permuting all cell labels. The statistical significance scores (interaction: 1; no significance: 0; avoidance: −1) were returned and normalized by Z score to develop the heatmap.

Cellular neighborhood identification and Voronoi diagram generation

To perform neighborhood analysis, we first captured "windows" across all images and cell phenotype, consisting of the 20 nearest neighboring cells based on the cells' centroids. These "windows" were subsequently clustered using Python's *scikit-learn* implementation of MiniBatchKMeans with $k = 20$ to detect CNs, based on their cellular composition. Finally, the colored CNs would be specially overlaid on the original fluorescent images using Voronoi diagram, and the cell phenotype fraction per CN could be computed.

t-distributed Stochastic Neighbor Embedding (*t*-SNE)

All *t*-SNE plots were generated in Jupyter Notebook (version 1.0.0) using default parameters. Markers used for *t*-SNE analysis include CTLA4, LAG3, PD-1, PD-L1, TIM3, VISTA, BCL2, BTK, DLL3, Ki67, SLFN11, p53, CD45RO, and Vimentin. For visualization, expression data were normalized across all markers (Figure S6D).

Uniform Manifold approximation and projection (UMAP)

We employed UMAP in conjunction with unsupervised clustering approaches to annotate single cells from publicly available scRNA-seq data as well as from SMI CosMx sequencing in this study. Following dimensionality reduction with UMAP, we performed unsupervised clustering to partition the cells into distinct subpopulations. Leveraging graph-based algorithms and density-based approaches, we identified transcriptionally coherent clusters representing putative cell types or states. Furthermore, we utilized publicly available reference datasets from Chan et al. to facilitate robust annotations. Through systematic comparisons of gene expression signatures, we could map our clusters to well-characterized cell populations, enabling a deeper interpretation of the observed heterogeneity.

Pseudotime trajectory analysis

Monocle2 (version 2.30.0) was applied to determine the differentiation of five TC-related CNs (CN2, CN3, CN9, CN13, CN17) with potential developmental relationship. For the neighborhoods, five lineage markers (PanCK, ASCL1, NEUROD1, POU2F3, YAP1) were selected to cell ordering. DDRTree (version 0.1.5) was used to learn tree-like trajectories after removing the batch effect of different samples.

Correlation of cellular neighborhood with genomic features

Associations between CNs and copy number variations (CNAs) were tested separately for gains and deletions and a similar strategy was used for gene mutations. We fit generalized linear models for each CN (under a binomial distribution with a logit link function), where the dependent variable was the proportion of CNs. Genes with fewer than three mutations observed were excluded from association analyses. Tests for association with copy number status were limited to genes designated as "amplifications" or "large deletions" within the COSMIC database,[78] and those associated with immune cytolytic activity.[42]

Cell ColonyMap analysis

We developed an algorithm to recognize the colony distribution of each cell phenotype. The specific steps for colony analysis in each core were as follows.

Cancer Cell
Article

♂ CellPress

(1) The area and coordinate set of each cell phenotype are separately extracted from the core.
(2) Individual projection of spatial distribution and size for each cell phenotype onto a blank layer. To streamline computations, the size of each cell phenotype is uniformly set to the median size across all cells of that type.
(3) Recognition of the contours of individual cell colonies. Refer to the "Code availability" section for further details.
(4) Projection of the contour sets of all individual cell phenotypes onto a single image for subsequent analysis. For quantification of the interaction strength between cell types A and B, three metrics were designed:

$$Area\,(A \cap B) \,=\, Overlap\;Area\,(A \cap B)$$

$$Proportion\,(A \cap B) \,=\, \frac{Overlap\;Area\,(A \cap B)}{Area\,(B)}$$

$$Proportion\,(B \cap A) \,=\, \frac{Overlap\;Area\,(A \cap B)}{Area\,(A)}$$

ColonyMap performance evaluation

To assess the accuracy of ColonyMap, we tested the performance in tumor boundaries identification across randomly selected 50 cores, using the results manually annotated by pathologists as the gold standard. Colonymap was compared with a commonly used artificial neural network-multilayer perceptron (ANN-MLP) model. The pixel count within the delineated contours was used for subsequent metric calculations. Specifically, true positives (TP) were defined as the number of pixels where both the test method and manual annotation identified a positive region. Similarly, we calculated false positives (FP) and false negatives (FN). It was noteworthy that true negatives were excluded from further calculations due to their dependence on the size of the background canvas. We applied widely adopted model evaluation metrics for comparison, including:

$$Sensitivity \,=\, \frac{TP}{TP+FN}$$

$$Precision \,=\, \frac{TP}{TP+FP}$$

$$F1\_score \,=\, 2 \times \frac{Precision \times Sensitivity}{Precision+Sensitivity}$$

Immunotherapy response evaluation

According to the Response Evaluation Criteria in Solid Tumor (RECIST) v1.1, patients with a complete response (CR) or partial response (PR) or stable disease (SD) to anti-PD-L1 antibody (atezolizumab or durvalumab) lasting >24 weeks are considered as having a DCB. Cases showing progression of disease (PD) or SD lasting ≤24 weeks are considered as showing no NDB.

Survival analysis

Log rank tests were used to assess OS or RFS differences between specific clinical status or among SCLC molecular subtypes. Associations of cell-cell interaction or CN frequency with survival were conducted using Cox proportional-hazards regression models, adjusting for pathological TNM stages by including it as a covariate. During the calculation of immune infiltration, we first treated all immune cell types collectively as a single category. Then we used ColonyMap to calculate the area of all immune cell colonies to represent the intensity of immune infiltration. The median value was used to stratify high/low immune infiltration to perform survival analysis. OS was calculated from the date of treatment to date of death or last known follow-up. RFS was calculated from the date of treatment to date of recurrence or last known follow-up.

Statistical analysis

All statistical analyses were conducted using GraphPad Prism (9.0.0), R (4.3.1), or Python (3.11.5). Normally distributed data were compared between two groups with the two-tailed Student's t test. Non-normal data were compared between two groups using the Mann-Whitney test. Multiple groups were compared using the Kruskal-Wallis test. Adjustment for multiple testing was conducted using the Benjamini–Hochberg test. $p < 0.05$ was considered significant unless otherwise indicated.